The Astrophysical Journal, 887:149 (17pp), 2019 December 20 https://doi.org/10.3847/1538-4357/ab54ce

Origins of Molecular Clouds in Early-type Galaxies

Iu. V. Babyk[1,2,3], B. R. McNamara[1,2,4], P. D. Tamhane[1,2], P. E. J. Nulsen[5,6], H. R. Russell[7], and A. C. Edge[8]
[1] Department of Physics and Astronomy, University of Waterloo, Waterloo, ON N2L 3G1, Canada; ibabyk@uwaterloo.ca, babikyura@gmail.com
[2] Waterloo Institute for Astrophysics, University of Waterloo, Waterloo, ON N2L 3G1, Canada
[3] Department for Extragalactic Astronomy and Astroinformatics, Main Astronomical Observatory of the National Academy of Sciences of Ukraine, 27 Zabolotnoho Str., 03143, Kyiv, Ukraine
[4] Perimeter Institute for Theoretical Physics, 31 Caroline Street N, Waterloo, ON N2L 2Y5, Canada
[5] Harvard-Smithsonian Center for Astrophysics, 60 Garden Street, Cambridge, MA 02138, USA
[6] ICRAR, University of Western Australia, 35 Stirling Highway, Crawley, WA 6009, Australia
[7] Institute of Astronomy, Madingley Road, Cambridge CB3 0HA, UK
[8] Department of Physics, University of Durham, South Road, Durham DH1 3LE, UK
Received 2018 October 24; revised 2019 October 30; accepted 2019 November 4; published 2019 December 17

Abstract

We analyze *Chandra* observations of the hot atmospheres of 40 early spiral and elliptical galaxies. Using new temperature, density, cooling time, and mass profiles, we explore relationships between their hot atmospheres and cold molecular gas. Molecular gas mass correlates with atmospheric gas mass and density over four decades from central galaxies in clusters to normal giant ellipticals and early spirals. The mass and density relations follow power laws: $M_{\rm mol} \propto M_{\rm X}^{1.4\pm0.1}$ and $M_{\rm mol} \propto n_{\rm e}^{1.8\pm0.3}$, respectively, at 10 kpc. The ratio of molecular gas to atmospheric gas within a 10 kpc radius lies between 3% and 10% for early-type galaxies and between 3% and 50% for central galaxies in clusters. Early-type galaxies have detectable levels of molecular gas when their atmospheric cooling times fall below ∼1 Gyr at a radius of 10 kpc. A similar trend is found in central cluster galaxies. We find no relationship between the ratio of the cooling time to free-fall time, $t_{\rm c}/t_{\rm ff}$, and the presence or absence of molecular clouds in early-type galaxies. The data are consistent with much of the molecular gas in early-type galaxies having condensed from their hot atmospheres.

Unified Astronomy Thesaurus concepts: Galaxy kinematics (602); Galaxy dynamics (591)

1. Introduction

Elliptical galaxies were historically thought to be devoid of gas. However, modern studies have shown that many early-type galaxies (ETGs) contain gas at broad range of temperatures. Most abundant are the hot, 10-million-degree atmospheres observed in X-rays (Forman et al. 1985; Trinchieri & Fabbiano 1985; Mathews & Brighenti 2003; Kim & Fabbiano 2015). Their X-ray luminosity scales with temperature as $L_{\rm X} \propto T^{4.5}$ (Boroson et al. 2011; Kim & Fabbiano 2013; Babyk et al. 2018a), indicating a strong link between atmospheric luminosity and halo mass (Forbes et al. 2017). Their hot atmospheres likely formed primarily from cool gas that accreted early and was heated to the virial temperature by shocks and by gas expelled from stars (Goulding et al. 2016).

Ellipticals and early spirals contain modest levels of molecular and atomic hydrogen. Dust is commonly seen in the form of clouds and lanes near to the nucleus (Sadler & Gerhard 1985; Goudfrooij et al. 1994; van Dokkum & Franx 1995). Dust is usually associated with larger quantities of cold atomic and molecular gas (Combes et al. 2007). Thirty to forty percent of ETGs contain detectable levels of molecular gas (Combes et al. 2007; Salomé et al. 2011; Young et al. 2011). Infrared and radio observations indicate that a minority of systems with relatively large amounts of molecular gas form stars at rates of $\lesssim 0.1\ M_{\odot}\ {\rm yr}^{-1}$ or so (Combes et al. 2007; Shapiro et al. 2010; Ford & Bregman 2013).

Neutral hydrogen is less abundant than molecular hydrogen in ETGs. In a study of 33 ETGs from the SAURON sample, H I is detected at a level of $10^6\ M_{\odot}$ in two-thirds of field galaxies. Detections plunge to 10% in cluster galaxies (Oosterloo et al. 2010; Pulatova et al. 2015). Like galaxies detected in CO, fast-rotating galaxies are more likely to harbor H I than slow rotators. Detection is a strong function of environment. Isolated galaxies are more likely to harbor H I than those in clusters. This implies that galaxies are either stripped of their H I or are unable to accrete material from their surroundings within clusters, or both. However, the prevalence of dynamically young H I structures connecting to disks suggests that at least some gas is accreted externally (Oosterloo et al. 2010).

The origin of cold gas in ETGs has been debated for decades. Its origin is key to understanding how ETGs formed and coevolved with massive nuclear black holes, why so few are experiencing significant levels of star formation, and if or how they are maintained by active galactic nucleus (AGN) feedback (Kormendy & Ho 2013). The absence of correlation between molecular gas mass and the host's stellar mass is inconsistent with mass loss from stars in the galaxy (Combes et al. 2007). However, the similarity between nebular gas metallicities, which are likely associated with molecular clouds, and stellar metallicity in four ETGs is consistent with an internal origin including stellar mass loss and/or cooling from the hot atmosphere but is inconsistent with having accreted from other galaxies (Griffith et al. 2019). On the other hand, counterrotation between stars and cold gas found in some systems and the prevalence of molecular gas in fast rotators (Young et al. 2011) may imply an external origin, perhaps due to mergers of gas-rich companions.

Taking a fresh approach, Werner et al. (2014) studied [C II] 157 μm, [O I] 63 μm, and [O Ib] 145 μm emissions in eight giant ellipticals and BCGs. They compared this emission to their atmospheric properties. This microwave line radiation emerges from warm molecular, neutral, or ionized gas at a temperature of ∼100 K that is associated with nebular emission. Comparing the molecular gas emission to their

atmospheric properties, Werner found stronger emission lines in systems with lower atmospheric gas entropy and shorter cooling times. In newer work, Lakhchaura et al. (2018) found a similar connection between nebular emission and cooling hot atmospheres, indicating a close connection between the hot atmosphere and molecular gas.

In this respect, ETGs appear similar to brightest cluster galaxies (BCGs), but scaled down to much lower molecular gas masses. BCGs, the elliptical-like galaxies at the centers of clusters, often contain reservoirs of cold molecular gas with masses lying between $10^9\,M_\odot$ and several $\times\ 10^{11}\,M_\odot$ (Edge 2001; Salomé & Combes 2003). The molecular gas masses correlate with nebular emission (Edge 2001), which is known to be associated with so-called cool cores, the cooling central regions of galaxy cluster atmospheres (Hu et al. 1985; Heckman et al. 1989; Crawford et al. 1999; Cavagnolo et al. 2008; McDonald et al. 2010). Like nebular emission and star formation (Rafferty et al. 2008), molecular gas is known to form in systems when the cooling time of the hot atmosphere falls below a cooling time threshold of $\sim 10^9$ yr within an altitude of approximately 10 kpc (Pulido et al. 2018). The existence of this threshold, in addition to other trends between molecular gas mass and atmospheric mass and density (Pulido et al. 2018), indicates that molecular gas condensed out of the hot atmospheres.

Atacama Large Millimetre Array (ALMA) has observed nearly a dozen central galaxies in groups and clusters (David et al. 2014; McNamara et al. 2014; Russell et al. 2014, 2016, 2017a, 2017b; Tremblay et al. 2016; Vantyghem et al. 2016, 2017; Simionescu et al. 2018). ALMA images show that much of the molecular gas lies outside of the nucleus in most systems. The gas appears in wisps and filaments traveling at slower velocities than the average speeds of the stars. Circumnuclear disks are rare. In many systems the molecular gas lies below and appears to have been drawn up behind the rising X-ray bubbles, as was noted in Perseus a decade ago (Fabian et al. 2003; Hatch et al. 2006; Salomé et al. 2011; Hlavacek-Larrondo et al. 2015; Yang & Reynolds 2016). This suggests two scenarios: preexisting molecular gas is drawn up by the bubbles, or low-entropy, keV atmospheric gas is drawn up behind the bubbles and cools in their wakes (Salomé et al. 2011).

Recognizing the difficulty of lifting high-density molecular clouds, McNamara et al. (2016) proposed that the keV gas becomes thermally unstable and cools behind the bubbles when the ratio of the cooling time to the timescale to fall back to the galaxy approaches unity, $t_c/t_I \lesssim 1$. The infall time is determined by the lesser of the free-fall and terminal speeds of the thermally unstable gas. This model emerged from ALMA observations and early observations of the Perseus Cluster (Russell et al. 2017a). Furthermore, *Chandra* observations have shown that atmospheric gas is lifted behind rising X-ray bubbles with displaced masses comparable to the molecular gas masses of their hosts (Fabian et al. 2002; Simionescu et al. 2010; Gitti et al. 2011; Werner et al. 2012; Kirkpatrick & McNamara 2015). Thermally unstable cooling in uplifted gas is seen in simulations (Revaz et al. 2008; Li & Bryan 2014).

This model implies a tight link between molecular gas and AGN feedback where the same process that heats and stabilizes the atmosphere creates its own cold fuel that feeds the AGN (Gaspari et al. 2012). The self-generation of cold gas would sustain radio mode feedback (McNamara et al. 2016).

How molecules residing in the atmospheres of ETGs formed is poorly understood. They may have arrived externally via mergers or inflowing cold filaments. They may have condensed internally from a combination of thermalized stellar ejecta and their hot atmospheres. Molecular cloud formation in disk galaxies is thought to be catalyzed primarily on dust grains (Le Bourlot et al. 2012). However, unshielded dust may be sputtered away in the harsh atmospheric environment of ETGs (Draine & Salpeter 1979), making it difficult to survive a merger and perhaps more difficult to form from cooling atmospheres. Nevertheless, despite the harsh atmospheric conditions, dust features are prevalent in ETGs, particularly in systems rich in molecular clouds (Russell et al. 2019; Werner et al. 2019). Upward of $10^{10}\ M_\odot$ of molecular gas is observed in BCGs (Edge 2001) which could not have originated in mergers (Pulido et al. 2018). Molecular clouds are apparently able to form and survive in these systems despite harsh atmospheric environments.

Here we analyze the thermodynamic properties of the hot atmospheres of 40 ETGs from *Chandra* archival data. Temperature, density, entropy, cooling time, mass, and free-fall time profiles are measured. The onset of thermally unstable cooling is investigated in the context of the molecular gas reservoirs and their role in the AGN feedback. Archival ALMA data are used to examine the molecular gas structure in some systems. We combine this study with the Pulido et al. (2018) sample of cluster BCGs with molecular gas to study trends between normal ellipticals and central galaxies in clusters over a large range in halo mass and molecular gas mass.

The paper is organized as follows. In Section 2 we describe our sample and data reduction of the *Chandra* observations. In Section 3 we present physical characteristics of the targets, including temperature, density, entropy, cooling, mass, and free-fall time profiles. In Section 4 we study t_c/t_{ff} to explore recently presented theoretical models of thermally unstable gas. In Section 5 we present correlations between molecular gas mass and X-ray gas properties. Conclusions are presented in Section 6.

We adopt the following cosmological parameters: $H_0 = 70\,\mathrm{km\,s^{-1}\,Mpc^{-1}}$, $\Omega_\Lambda = 0.7$, and $\Omega_M = 0.3$.

2. Sample and Data Reduction

2.1. Sample Selection

Our sample was selected from Babyk et al. (2018a), which includes 94 relatively nearby ETGs (brightest group galaxies, and early spiral galaxies) observed with the *Chandra X-ray Observatory*. The sample is intended to investigate X-ray scaling relations, structural properties, and dynamical properties of ETGs over a large range in mass (Hogan et al. 2017a, 2017b; Main et al. 2017; Pulido et al. 2018). The challenge of assembling spatially resolved profiles of lower-mass early-type systems concerns low count rates and relatively short exposure times. Previous studies focused on the 10–15 brightest galaxies and groups (see, e.g., Werner et al. 2013). Recently, Lakhchaura et al. (2018) presented the spatial analysis of 49 ETGs. Here we examine 40 ETGs with a sufficient number of photon events to extract at least four concentric annular bins. The sample spans temperatures of $\sim$0.2–2.5 keV, X-ray luminosities of $L_X \sim 10^{37}$–10^{42} erg s^{-1},

and radio luminosities of $L_R \sim 10^{35}$–10^{42} erg s^{-1} corresponding to estimated jet powers of $P_{jet} \sim 10^{40}$–10^{45} erg s^{-1}. Redshifts lie in the range of $z \sim 0.001$–0.032.

Interpreting trends based on archival analyses can be perilous owing to the poorly defined selection function. The targets tend to be relatively bright in X-rays and were selected for observation based on heterogeneous criteria. This concern is lessened to some degree by cross-correlating the X-ray observations with molecular gas data taken from the ATLAS^{3D} catalog, which has a well-defined selection function. ATLAS^{3D} molecular gas masses and upper limits were measured with single-dish IRAM observations (Young et al. 2011). The ATLAS^{3D} objects were then cross-correlated with the ETGs in Babyk et al. (2018a, 2018b) to form the sample presented here. The ATLAS^{3D} is a complete sample of ETGs brighter than $M_K = -21.5$ within a distance of 42 Mpc (Young et al. 2011).

Single-dish CO measurements from Edge (2001), subsequently analyzed by Pulido et al. (2018), form the cluster central galaxy sample that we compare to the ETG sample. The Edge sample selected central galaxies in cooling cores with Hα emission above $L_{H\alpha} = 10^{39}$ erg s^{-1}. Thus, the Edge selection differs from ATLAS^{3D}, which will limit the conclusions that can be drawn. Nevertheless, the samples combined allow us to examine, for the first time, relationships between molecular gas and hot atmospheres over a wide range of halo mass. This is a significant step. Other studies have focused on the relationship between molecular gas and the stellar content and their dynamics (Young et al. 2008; Emsellem et al. 2001, 2011), or the relationship between atmospheric properties, the stars, and the central black hole (Ma et al. 2014). This study extends our work on central galaxies in clusters, whose molecular gas is closely tied to their atmospheres (Edge et al. 2002; David et al. 2014, 2017; McNamara et al. 2014; Russell et al. 2014, 2015, 2017a; Tremblay et al. 2016; Vantyghem et al. 2017, 2018; Pulido et al. 2018), to lower-mass atmospheres and their parent halos.

Table 1 lists the sample, including target name, coordinates, *Chandra* observational ID, cleaned exposure time, morphology, galaxy classification, redshift, angular and luminosity distance, foreground hydrogen column density taken from Dickey & Lockman (1990), and radio flux. Properties are taken from NED,[9] SIMBAD,[10] and HyperLEDA[11] databases. We found a slight discrepancy in morphological definition between NED and SIMBAD. For example, NGC 507 and NGC 4382 are classified as SA0 galaxies in NED and S0 in SIMBAD. Our sample includes 11 BCGs. The angular and luminosity distances were defined using their redshift for the cosmology described above and, for some Virgo galaxies, using the surface brightness fluctuations (Mei et al. 2007; Cappellari et al. 2011).

2.2. Data Processing

Data reduction was done using CIAO version 4.8 and CALDB version 4.7.1 (see Hogan et al. 2017a; Babyk et al. 2018a for more details). *Chandra* observations were downloaded from the HEASARC[12] archive. Data processing of the event lists was performed with a custom-made pipeline XPIPE (Fruscione et al. 2006). The reprocessing and rescreening of data by creating new bad pixel files and level 2 event files were achieved using the `chandra_repro` task. The correction of time-dependent gain was applied using the `acis_process_events` task. Background flares were flagged and removed using the `lc_clean` task provided by M. Markevitch. Periods of anomalously high backgrounds were excluded. Cosmic-ray afterglows were removed using the `acis_detect_afterglow` task. Multiple observations were reprojected to the position of the observation with the longest exposure time. Each observation was processed with the appropriate blank-sky background file, which was normalized and reprojected to the corresponding position. Each observation includes a 0.3–6.0 keV energy band. For multiple observations, the images were summed and backgrounds were subtracted. The `wavdetect` routine was applied to detect and remove point sources.

2.3. Spectral Extraction and Modeling

Source and background spectra were extracted individually for each observation. The ancillary response and response matrix files were generated using the MKWARF and MKACISRMF tools. The spectra were grouped with at least 20 counts per energy bin using the FTOOLS task GRPPHA. Corrections for chip gaps and the area lost to point sources were corrected using exposure maps.

Spectral analysis was done with XSPEC version 12.9.1 (Arnaud 1996). The spectral fitting included an absorbed, single-temperature, multicomponent model PHABS*(APEC+PO+MEKAL+PO) to correct for unresolved, low-mass X-ray binaries (LMXBs), active binaries (AB), and cataclysmic variables (CVs). The APEC component (Smith et al. 2001) describes the emission of hot gas, while the first PO and set of MEKAL+PO models (Mewe et al. 1986; Kaastra & Mewe 1993; Liedahl et al. 1995) fit the possible contribution of the X-ray emission of LMXBs and AB+CV sources, respectively. The hydrogen column density, N_H, was fixed as given in Table 1.

Metallicity in the APEC model was fixed at 0.5 $Z_\odot$. We also perform the spectral fitting with free N_H. We find that the best-fit N_H for about 40% our sample is higher by a factor of 1.5–2 compared to those obtained by Dickey & Lockman (1990) and is in agreement with more recent measurements of Kalberla et al. (2005). However, the best-fit temperature and normalization are unaffected by this discrepancy. The parameters of additional spectral components that were added to represent the emission of LMXBs and stellar sources emission were fixed (see, e.g., Babyk et al. 2018a, for more details of the presented spectral model, and Boroson et al. 2011; Wong et al. 2014, for other multicomponent spectral models). The spectra were fitted in the 0.3–6.0 keV energy range, which provides an optimal ratio of the galaxy and background flux for *Chandra* observations. Multiple spectra for the same annulus were fitted simultaneously. Uncertainties were determined using XSPEC `error` quoted for 1σ confidence. Quoted uncertainties are statistical.

3. Galaxy Properties

Here we present profiles of temperature, density, cooling, mass, and free-fall time for the range of radii ~0.1–50.0 kpc. Analysis of entropy profiles is presented in Babyk et al. (2018b). The multicomponent spectral model described above

[9] https://ned.ipac.caltech.edu/
[10] http://simbad.u-strasbg.fr/
[11] Lyon-Meudon Extragalactic Database.
[12] http://heasarc.gsfc.nasa.gov/

Table 1
Early-type Galaxies/Faint Groups Sample

Name	R.A. (J2000) (2)	Decl. (J2000) (3)	ObsIDs (4)	Exposure (ks) (5)	Type (6)	BCG (7)	z (8)	D_A (Mpc) (9)	D_L (Mpc) (10)	N_H (10^{20} cm^2) (11)	1.4 GHz Flux (mJy) (12)
IC 1262	17:33:02.022	+43:45:34.51	6949, 7321, 7322	36.02, 34.98, 35.17	E	√	0.032649	133.0	141.8	2.47	16.4 ± 1.0
IC 1459	22:57:10.608	−36:27:43.997	2196	45.14	E3		0.006011	25.503	25.8	1.19	1279.7 ± 45.2
IC 4296	13:36:39.053	−33:57:57.30	2021, 3394	19.27, 20.78	E		0.012465	52.358	53.7	4.11	546.6 ± 17.8
NGC 315	00:57:48.883	+30:21:08.812	4156	39.49	E		0.016485	68.816	71.1	5.87	772.1 ± 25.3
NGC 499	01:23:11.459	+33:27:36.30	10536	18.33	E		0.014673	61.423	63.2	5.26	62.7 ± 1.9
			10865	5.12							
			10866	8.01							
			10867	7.02							
NGC 507	01:23:39.950	+33:15:22.22	317	40.30	E	√	0.016458	68.706	71.0	5.32	61.7 ± 2.5
NGC 533	01:25:31.432	+01:45:33.57	2880	28.40	E3		0.018509	77.025	79.9	3.12	28.6 ± 1.0
NGC 708	01:52:46.482	+36:09:06.53	2215, 7921	28.75, 108.63	E	√	0.016195	67.635	69.8	5.37	65.7 ± 2.3
NGC 720	01:53:00.523	−13:44:19.25	7372	49.13	E5		0.005821	24.704	25.0	1.55	96.2 ± 3.4
			7062	22.12							
			8448	8.06							
			8449	18.91							
NGC 741	01:56:20.959	+05:37:43.77	2223	28.14	E0		0.018549	77.186	80.1	4.47	478.8 ± 16.2
NGC 1316	03:22:41.789	−37:12:29.52	2022	21.21	E		0.005871	24.914	25.2	1.92	254.7 ± 9.9
NGC 1332	03:26:17.321	−21:20:07.33	2915, 4372	4.10, 16.38	S0		0.005084	21.601	21.8	2.29	4.6 ± 0.5
NGC 1399	03:38:29.083	−35:27:02.67	9530	56.98	E1	√	0.004753	20.205	20.4	1.31	208.0 ± 6.9
NGC 1404	03:38:51.917	−35:35:39.81	16233	91.94	E1		0.006494	27.531	27.9	1.35	3.9 ± 0.6
			16231	56.09							
			16232	64.03							
			16234	84.64							
NGC 1407	03:40:11.904	−18:34:49.36	14033	50.26	E0		0.005934	25.179	25.5	5.41	87.7 ± 3.5
NGC 1550	04:19:37.921	+02:24:35.58	5800, 5801	44.55, 44.45	E2	√	0.012389	52.045	53.3	11.2	16.6 ± 1.6
NGC 3091	10:00:14.125	−19:38:11.32	3215	27.34	E3	√	0.013222	55.473	56.9	4.75	2.5 ± 0.5
NGC 3923	11:51:01.783	−28:48:22.36	9507	80.90	E4		0.005801	24.620	24.9	6.29	31.2 ± 1.1
NGC 4073	12:04:27.059	+01:53:45.65	3234	25.76	E	√	0.019584	81.364	84.6	1.90	17.1 ± 1.0
NGC 4104	12:06:38.910	+28:10:27.17	6939	34.86	S0	√	0.028196	115.60	122.2	1.68	7.3 ± 0.5
NGC 4125	12:08:06.017	+65:10:26.88	2071	52.97	E6		0.004523	19.234	19.4	1.86	24.9 ± 1.2
NGC 4261	12:19:23.216	+05:49:29.695	9569	102.24	E2		0.007378	31.236	31.7	1.56	4066.7 ± 124.0
NGC 4325	12:23:06.672	+10:37:17.05	3232	28.30	E4	√	0.025714	105.80	111.3	2.18	4.1 ± 0.5
NGC 4374	12:25:03.743	+12:53:13.19	5908, 6131	44.04, 35.81	E1		0.003392	16.422	18.1	2.58	27.5 ± 2.0
NGC 4382	12:25:24.053	+18:11:27.89	2016	29.33	S0		0.002432	16.265	17.7	2.51	8.0 ± 0.5
NGC 4472	12:29:46.798	+08:00:01.48	11274	39.67	E2		0.003272	15.621	17.1	1.65	219.9 ± 7.8
NGC 4552	12:35:39.8	+12:33:23	13985	49.41	E		0.001134	15.523	16.1	2.56	100.1 ± 3.0
			14358	49.41							
			14359	47.11							
NGC 4636	12:42:49.867	+02:41:16.01	3926, 4415	67.26, 66.17	E0		0.003129	13.335	13.4	1.83	77.8 ± 2.8
NGC 4649	12:43:40.008	+11:33:09.40	8182, 8507	45.87, 15.73	E2		0.003703	15.767	15.9	2.13	29.1 ± 1.3
NGC 4696	12:48:49.277	−41:18:39.92	1560	21.20	E1	√	0.009867	41.613	42.4	8.07	24.4 ± 6.0
NGC 4782	12:54:35.698	−12:34:06.92	3220	49.33	E0		0.015437	64.545	66.6	3.56	3.1 ± 0.4
NGC 5044	13:15:23.969	−16:23:08.00	17195	77.01	E0	√	0.00928	39.173	39.9	5.03	34.7 ± 1.1
			17196	85.80							
			17653	32.46							
			17654	24.01							
			17666	82.79							
NGC 5353	13:53:26.7	+40:16:59.0	14903	37.20	S0		0.007755	32.813	33.3	0.98	40.5 ± 1.3
NGC 5813	15:01:11.265	+01:42:07.09	12952	140.00	E1		0.006525	27.662	28.0	4.23	14.8 ± 1.0
			12951	71.95							
			12953	31.76							
			13246	45.02							
			13247	34.08							

Table 1
(Continued)

Name	R.A. (J2000) (2)	Decl. (J2000) (3)	ObsIDs (4)	Exposure (ks) (5)	Type (6)	BCG (7)	z (8)	D_A (Mpc) (9)	D_L (Mpc) (10)	N_H (10^{20} cm^2) (11)	1.4 GHz Flux (mJy) (12)
			13255	43.34							
NGC 5846	15:06:29.253	+01:36:20.29	7923	85.25	E	√	0.00491	20.867	21.1	4.24	21.0 ± 1.3
NGC 6338	17:15:23.0	+57:24:40.0	4194	44.52	E5		0.027303	112.10	118.3	2.55	57.0 ± 1.8
NGC 6482	17:51:48.833	+23:04:18.88	3218	10.03	E		0.013129	55.091	56.5	8.04	3.2 ± 0.1
NGC 6861	20:07:19.482	−48:22:12.94	11752	88.89	SA0		0.009437	39.826	40.6	4.94	40.7 ± 2.0
NGC 7618	23:19:47.212	+42:51:09.65	16014	121.00	E		0.017309	72.164	74.7	11.9	38.3 ± 2.0
UGC 408	00:39:18.578	+03:19:52.87	11389	93.80	SAB		0.014723	61.628	63.5	2.80	980.0 ± 30.9

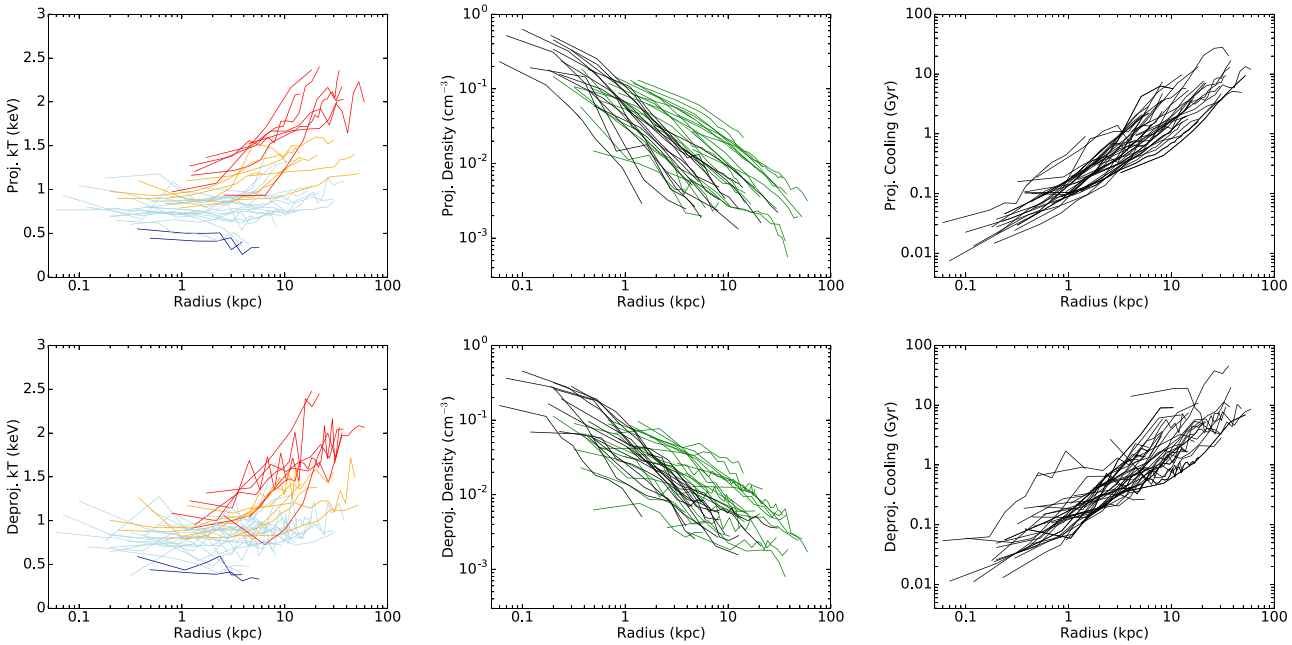

Figure 1. Projected (top) and deprojected (bottom) temperature, density, and cooling time profiles (from left to right) for the entire sample of low-mass systems. For clarity we plot temperature profiles using four colors. Dark-blue temperature curves show profiles with average temperature in the range of 0.2–0.5 keV; light-blue, 0.5–1.0 keV; orange, 1.0–1.5 keV; and red, 1.5–2.5 keV. Density profiles are indicated by shape. Those characterized by power laws of the form $\beta = 1.5$–2.0 are indicated in black. Density profiles with cores, $\beta = 1.0$–1.5, are indicated in green. We removed error bars for clarity.

was applied, and the output temperature and normalization parameter of the APEC model were extracted. The X-ray emission from each extraction annulus includes emission from other hotter annuli at higher altitudes. Therefore, the emission must be "deprojected" to isolate the emission in the desired annulus from emission from overlying layers. For this the model-independent DSDEPROJ routine (Russell et al. 2008) was adopted. The deprojected spectra were then fitted using the multicomponent model mentioned above in the same way as projected spectra.

3.1. Temperature, Density, and Cooling Time Profiles

In the left panels of Figure 1 we plot temperature profiles before (top) and after (bottom) deprojection. For clarity we plot profiles using four colors. Dark-blue lines show profiles with average temperature in the range of 0.2–0.5 keV; light-blue, 0.5–1.0 keV; orange, 1.0–1.5 keV; and red, 1.5–2.5 keV. Error bars are omitted for clarity. The projected and deprojected temperature profiles show significant variations. Galaxies with average temperatures below 1.5 keV tend to rise in temperature toward their centers. This may be due to shock activity, which raises the entropy of the central atmospheres of ellipticals and some BCGs (Werner et al. 2012). Flat temperature profiles are seen in others. The red temperature profiles indicate systems with sharp temperature increases (by a factor of 1.5 and higher within just several kiloparsecs) beyond ∼10 kpc. Such a quick rise is probably associated with the hot intracluster medium since this rise is only observed in BCGs.

Density profiles were constructed using the spectral temperature and normalization (N) parameters. The projected and deprojected electron number density profiles were derived as

$$n_e = D_A(1+z)10^7\sqrt{\frac{4\pi\ N\ 1.2}{V}}, \quad (1)$$

where the factor of 1.2 was defined using the ionization ratio n_e/n_p, V is the volume of concentric annular region in cm^3, D_A is the angular diameter distance, and N is the normalization, which is proportional to the integrated emission measure. Density profiles follow $n_e \propto r^{-\beta}$, with $\beta \approx 1.0$–2.0. The middle panels of Figure 1 show the radial distribution of projected and deprojected electron densities. Density profiles

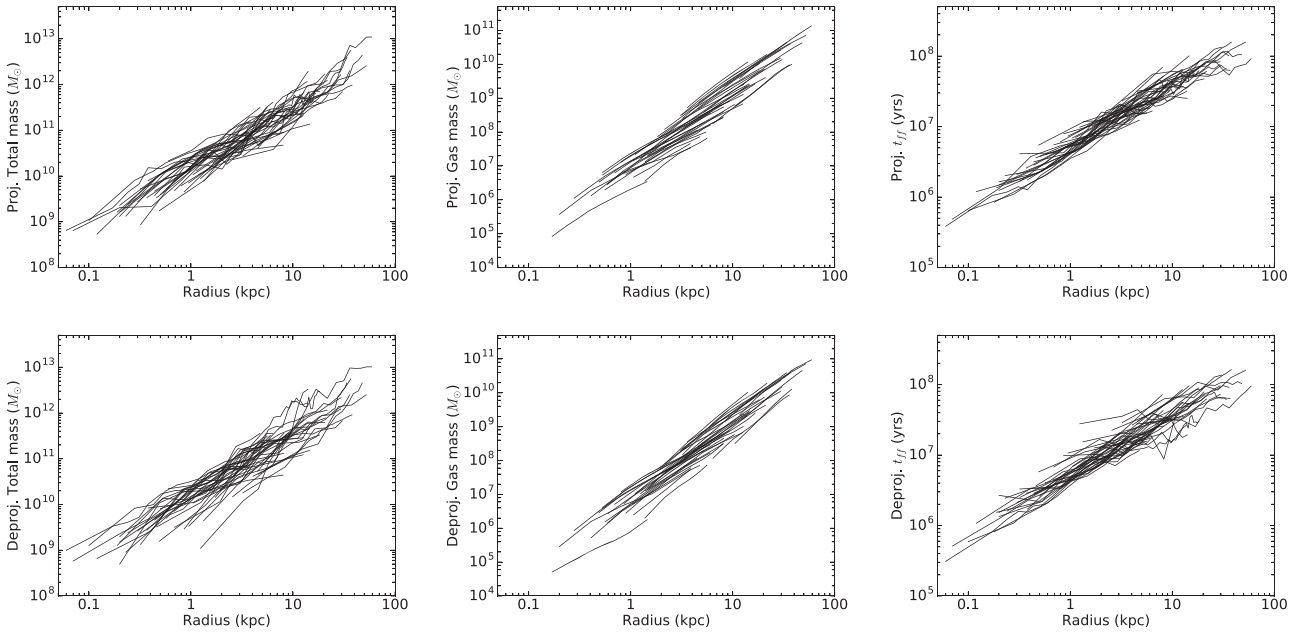

Figure 2. Projected (top) and deprojected (bottom) total and gas mass profiles with the free-fall time profiles for the entire sample of low-mass systems. We removed error bars for clarity.

are indicated by shape. Those characterized by power laws of the form $\beta = 1.5$–2.0 are indicated in black. Profiles with cores, $\beta = 1.0$–1.5, are indicated in green. The galaxies with X-ray power-law density profiles (black lines) correspond to lower temperature atmospheres with $T = 0.3$–1.0 keV. Core profiles in green are associated with hotter atmospheres $T \gtrsim 1$ keV. The central projected densities are 10%–30% higher than deprojected profiles.

The hot atmosphere radiates its thermal energy on the cooling timescale given by

$$t_{\rm c} = \frac{3{\rm P}}{2n_e n_{\rm H}\Lambda(Z,\,T)} \approx \frac{3PV}{2L_X}. \tag{2}$$

This is the thermal energy of the gas, $E_{\rm thermal} = PV$, divided by the energy lost per unit volume. Here $\Lambda(Z,\,T)$ is the cooling function that depends on metallicity and temperature. $P = 2n_{\rm e}k_{\rm B}T$ is the pressure, and $L_{\rm X}$ is the X-ray luminosity. First, we extracted X-ray flux of the galaxies by integrating the multicomponent model between the 0.1 and 100 keV energy band. Then, an estimated X-ray flux was used to derive the bolometric X-ray luminosity as $L_{\rm X} = 4\pi D_{\rm L}^2 \times$ flux. The projected and deprojected cooling time profiles are shown in the right panels of Figure 1. The cooling time of the entire sample lies below $t_{\rm c} \lesssim 10^9$ yr at $\lesssim$10 kpc. The largest cooling time is 14.04 ± 2.31 Gyr within the innermost region ($\sim$4.05 kpc) in UGC 408, while the lowest one is about 0.01 Gyr at 0.1 kpc in the IC 1459 and NGC 1332 targets.

3.2. Mass and Free-fall Time Profiles

3.2.1. The Gas and Total Mass

We use assumptions of hydrostatic equilibrium and spherical symmetry of hot gas in the gravitational potential (see, e.g., Navarro et al. 2010; Babyk & Vavilova 2012, 2013; Babyk et al. 2014; Vavilova et al. 2015; Babyk 2016) to calculate the total mass profiles. The derived temperature and density profiles were used to estimate projected and deprojected total mass as

$$M_T(r) = -\frac{k_{\rm B}T(r)r}{G\mu m_{\rm p}}\left(\frac{d\ln n_e}{d\ln r} + \frac{d\ln T}{d\ln r}\right), \tag{3}$$

where $\mu = 0.62$ is the mean particle mass in units of proton mass, $k_{\rm B}$ is the Boltzmann constant, G is the gravitational constant, and $m_{\rm p}$ is the proton mass. The projected and deprojected total mass profiles for the entire sample of low-mass systems are given in the left panels of Figure 2. The two sets of mass profiles are consistent with one another, and they show a scatter of $\sim$20% in mass at a fixed radius. The total mass spans a range of $\sim 10^9$–$10^{13} M_\odot$ and $\sim$0.1–50.0 kpc in radius.

We derive gas mass profiles by integrating the gas density over the radius. The results of this integration are shown in the middle panels of Figure 2 for both projected and deprojected profiles. The gas mass profiles are similar, showing a scatter of only $\sim$15%. The gas mass spans six decades, $\sim 10^5$–$10^{11}\ M_\odot$. The gas fractions are small, about 1% at 10 kpc.

3.2.2. Free-fall Time

One aim of this paper is to understand the effect of mass in regulating the balance between cooling and heating in galaxy and cluster cores. We examine the role of mass in two ways. First, we evaluate correlations between molecular gas mass and the mass of various components of ETGs, such as atmospheric gas mass, stellar mass, and total mass within a given radius. Second, we look at acceleration, which is related to mass. The free-fall time profiles are useful because they are relevant to thermally unstable cooling of hot atmospheres. We derive free-fall time profiles using the total mass profiles to calculate acceleration, $g = (GM)/r^2$, as

$$t_{\rm ff}(r) = \sqrt{2r/g}\,. \tag{4}$$

Free-fall time profiles of the form (Equation (4)) can be directly compared to previous results in clusters. The right panels of Figure 2 show the projected and deprojected free-fall time profiles. They are consistent with each other, showing only ∼14% variation at 10 kpc. Free-fall time profiles have been measured for a large number of central galaxies in clusters (Hogan et al. 2017a, 2017b; Main et al. 2017; Pulido et al. 2018). These studies found, as we do here, a small variance in the free-fall time profiles. Furthermore, their values at 10 kpc, $\simeq 5 \times 10^7$ yr, found in cluster central galaxies are close to those found here for ETGs. This demonstrates that the mass profiles of BCGs and ETGs are similar in their inner few tens of kiloparsecs.

4. Thermally Unstable Atmospheric Cooling

Hot atmospheres are expected to become thermally unstable to linear density perturbations, when the ratio of the cooling time to free-fall time, t_c/t_{ff}, falls below unity (Nulsen 1986; Pizzolato & Soker 2005; McCourt et al. 2012). Hydrodynamical simulations of three-dimensional atmospheres apparently show that this instability criterion threshold may rise well above unity. Studies have claimed that thermally unstable cooling ensues from linear perturbations when t_c/t_{ff} falls below 10, fueling a self-regulating feedback loop (McCourt et al. 2012; Sharma et al. 2012; Gaspari & Churazov 2013; Li et al. 2015). However, later simulations by Choudhury & Sharma (2016) do not confirm the theoretical basis for the $t_c/t_{ff} < 10$ criterion. Furthermore, using a small number of systems, McNamara et al. (2016) showed that the observed ratio of t_c/t_{ff} is driven by the numerator, t_c, while the denominator, t_{ff}, adds noise (see Section 5.4 for more details). Since then, larger samples have been analyzed, paying careful attention to systematic biases, spanning a large range of halo mass. Analyses of t_c/t_{ff} profiles of clusters and their BCGs performed by Hogan et al. (2017b) and Pulido et al. (2018) showed no evidence that t_c/t_{ff} falls significantly below 10. They found that t_c/t_{ff} lies between 10 and 30 in systems with star formation and molecular clouds, with no indication that lower values of t_c/t_{ff} correlated with higher star formation rates or molecular gas masses. Consistent with Voit et al. (2015, 2019), they found a floor at $t_c/t_{ff} \sim 10$ rather than a threshold. While this floor may well be physically significant, they found that the range of t_c/t_{ff} values can be explained as an observational selection effect, raising uncertainty in its interpretation.

In Figure 3 we plot profiles of the deprojected ratio t_c/t_{ff}. We find that the minima all lie between 10 and 30. While a few values dip below 10, these departures are consistent with measurement noise. Plotted in blue are the t_c/t_{ff} profiles for systems with CO detections. Plotted in green and red are CO upper limits below 10^8 and 10^7 $M_\odot$, respectively. The systems with CO detections do not segregate from those with CO upper limits. However, those that contain detectable levels of CO preferentially show lower cooling times, a topic discussed below.

5. Molecular Gas Distribution

The primary aim of this study is to understand the origin of molecular gas in the cores of low- and high-mass systems. Archival ALMA data are available for five galaxies in our sample, which we analyze here. We use previously published cold gas mass measurements for clusters and ETGs to explore possible relationships between atmospheric properties and molecular gas, as found in earlier studies of cluster central galaxies (Cavagnolo et al. 2008; Rafferty et al. 2008; Voit & Donahue 2015; Pulido et al. 2018). As most CO measurements of ETGs have yielded upper limits, we use the survival statistic to examine our relations. We also use a β-model (Cavaliere & Fusco-Femiano 1978; Babyk 2012; Babyk & Del Popolo 2014) fitting to calculate density and gas mass profiles of those galaxies with known masses of cold gas but with X-ray data too poor to construct spatially resolved gas mass profiles. The objects whose X-ray masses were estimated using the β-model are listed in Table 2. We follow Babyk et al. (2018a) to fit the X-ray surface brightness profiles and to estimate the total and gas mass profiles.

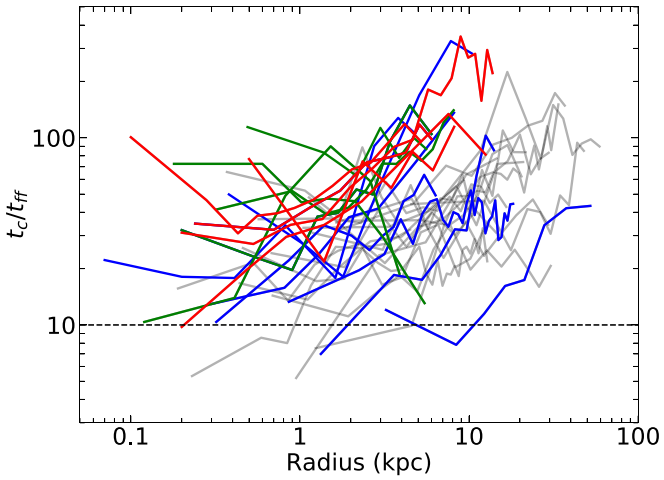

Figure 3. Deprojected t_c/t_{ff} profiles for the entire sample of ETGs. Error bars are deleted for clarity. Blue profiles are objects with CO detection. Red and green profiles are upper limits.

5.1. ALMA Data Reduction

We analyzed archival ALMA data for five galaxies from our sample. IC 1459, NGC 1332, and NGC 6861 were observed in ALMA band 6 to cover the CO (2–1) line emission, while NGC 1407 and NGC 4696 were observed in band 3 to cover the CO (1–0) line emission. A description of observational parameters is given in Table 3. The data were processed in CASA version 4.7.2 using the ALMA pipeline reduction scripts. We applied continuum phase self-calibration to each data set, which improved the image quality. The continuum for each galaxy was imaged using natural weighting. To isolate the molecular line emission, the continuum was subtracted using `uvcontsub`. The continuum-subtracted measurement sets were imaged using natural weighting for better sensitivity with 20 km s^{-1} channels. Integrated line emission maps were produced by integrating over all the channels containing line emission.

For NGC 4696, the spectrum was fitted with a single Gaussian profile to get line intensity. For NGC 1332 and NGC 6861, spectra were integrated numerically and the errors in the line intensity (σ_I) were estimated using the formula given in Young et al. (2011) as

$$\sigma_I^2 = (\Delta\nu)^2 \sigma^2 N_1 \left(1 + \frac{N_1}{N_b}\right), \quad (5)$$

Table 2
Early-type Galaxies of ATLAS^{3D} Sample

Name	R.A. (J2000) (2)	Decl. (J2000) (3)	ObsIDs (4)	Exposure (ks) (5)	Type (6)	z (7)	D_A (Mpc) (8)	D_L (Mpc) (9)	N_H (10^{20} cm^2) (10)	kT (keV) (11)	log(M_{mol}) ($M_\odot$) (12)	1.4 GHz Flux (mJy) (13)
IC 1024	14:31:27.221	+03:00:32.78	14901	20.07	S0	0.004933	20.96	21.2	2.55	0.46 ± 0.11	8.61 ± 0.02	24.7 ± 1.2
NGC 1266	17:45:35.288	−46:05:23.71	19498	80.06	Sb	0.007238	30.65	31.1	5.18	0.80 ± 0.03	7.58 ± 0.01	115.6 ± 3.5
NGC 2768	09:11:37.504	+60:02:13.95	9528	65.46	E6	0.004513	19.19	19.4	3.87	0.35 ± 0.02	7.64 ± 0.07	14.5 ± 0.6
NGC 3245	10:27:18.385	+28:30:26.63	2926	9.76	Sab	0.00423	13.827	13.9	2.08	0.55 ± 0.11	7.27 ± 0.12	6.7 ± 0.5
NGC 3599	11:15:26.949	+18:06:37.43	9556	20.16	S0	0.002799	11.93	12.0	1.42	0.36 ± 0.05	7.36 ± 0.08	2.3 ± 0.4
NGC 3607	11:16:54.657	+18:03:06.51	2073	39.00	E	0.003142	13.39	13.5	1.48	0.59 ± 0.11	7.42 ± 0.05	6.9 ± 0.4
NGC 3619	11:19:21.621	+57:45:27.66	19320	9.97	S0	0.005204	22.107	22.3	74.7	0.36 ± 0.14	8.28 ± 0.05	5.6 ± 0.5
NGC 3665	11:24:43.630	+38:45:46.05	3222	18.19	S0	0.006901	29.23	29.6	2.06	0.30 ± 0.05	8.91 ± 0.02	112.2 ± 3.7
NGC 4036	12:01:26.891	+61:53:44.52	6783	15.13	Sa	0.00462	19.64	19.8	1.89	0.46 ± 0.07	8.13 ± 0.04	11.6 ± 0.5
NGC 4203	12:15:05.054	+33:11:50.40	10535	42.18	Sa	0.003623	15.429	15.5	1.19	0.28 ± 0.03	7.39 ± 0.05	6.1 ± 0.5
NGC 4283	12:20:20.769	+29:18:39.16	7081	112.14	E	0.003522	15.0	15.1	1.77	0.35 ± 0.04	7.10 ± 0.09	385.0 ± 11.6
NGC 4459	12:29:00.026	+13:58:42.89	11784	30.18	S0	0.003976	16.92	17.1	2.67	0.54 ± 0.08	8.24 ± 0.02	2.7 ± 0.6
NGC 4476	12:29:59.081	+12:20:55.21	3717	20.83	S0	0.006565	27.83	28.2	2.54	0.35 ± 0.05	8.05 ± 0.04	245.6 ± 8.7
NGC 4477	12:30:02.172	+13:38:11.19	9527	38.18	S0	0.004463	18.98	19.2	2.63	0.34 ± 0.02	7.54 ± 0.06	6.2 ± 0.5
NGC 4526	12:34:03.029	+07:41:56.90	3925	44.11	S0	0.002058	16.5	17.5	1.65	0.37 ± 0.02	8.59 ± 0.01	12.0 ± 0.5
NGC 4596	12:39:55.954	+10:10:34.18	11785	31.38	Sa	0.006311	27.76	27.1	1.98	0.27 ± 0.05	7.31 ± 0.09	3.4 ± 0.6
NGC 4710	12:49:38.958	+15:09:55.76	9512	30.16	S0	0.003676	15.65	15.8	2.15	0.64 ± 0.06	8.72 ± 0.01	18.7 ± 1.0
NGC 5866	15:06:29.561	+55:45:47.91	2879	27.43	Sab	0.002518	14.9	15.2	1.45	0.41 ± 0.08	8.47 ± 0.01	21.8 ± 1.1
NGC 7465	23:02:00.952	+15:57:53.55	14904	30.06	Sb	0.006538	27.71	28.1	6.03	0.45 ± 0.10	8.79 ± 0.02	19.1 ± 1.1

Table 3
ALMA Observational Parameters and Results

Galaxy	Obs. Date	t_{obs} (min)	Synthesized Beam (arcsec × arcsec)	Frequency Range (GHz)	Bandwidth (GHz)	Velocity Resolution (km s^{-1})	PI	$S_{CO(2-1)}$ (Jy km s^{-1})	$S_{CO(1-0)}$ (Jy km s^{-1})	M_{mol} (10^7 $M_\odot$)
IC 1459	2016 Apr 11	11.6	1.04 × 0.80	225.6–244.5	5.9	2.56	Prandoni Isabella	<0.35	⋯	<0.08
NGC 1332	2014 Sep 1	22.3	0.32 × 0.24	226.4–246.1	5.9	1.28	Barth Aaron	38.72 ± 0.31	⋯	6.04 ± 0.05
NGC 1407	2016 May 3	15.0	1.50 × 1.08	112.1–115.3	4.9	81.14	Hodges-Kluck Edmund	⋯	<1.56	<1.06
NGC 4696	2016 Jan 27	77.7	2.29 × 1.74	99.3–115.0	7.6	5.22	Hamer Stephen	⋯	3.07 ± 0.26	5.79 ± 0.41
NGC 6861	2014 Sep 1	23.9	0.37 × 0.28	225.5–245.1	5.9	1.28	Barth Aaron	89.91 ± 1.62	⋯	48.72 ± 0.87

where $\Delta\nu$ is the velocity channel width, σ is the rms noise per channel, N_1 is the number of channels containing line emission, and N_b is the number of channels used to measure the baseline. For sources in which we do not detect any line emission, 3σ upper limits on integrated line intensities were estimated by extracting the spectrum within a 2 kpc $\times$2 kpc box centered at the optical centroid of the galaxies and following McNamara & Jaffe (1994),

$$S_{\rm CO}\Delta\nu = \frac{3\sigma_{\rm ch}\Delta V}{\sqrt{\Delta V/\Delta V_{\rm ch}}}\ {\rm Jy\ km\ s^{-1}}, \quad (6)$$

where $\sigma_{\rm ch}$ is the rms noise per channel in units of Jy; ΔV is the expected FWHM of the line, which we assume to be 200 km s^{-1}; and $\Delta V_{\rm ch}$ is the velocity channel width.

The molecular gas mass is calculated using integrated CO (1–0) line intensity as given in Solomon & Vanden Bout (2005) and Bolatto et al. (2013),

$$M_{\rm mol} = 1.05\times10^{4}\left(\frac{X_{\rm CO}}{2\times10^{20}\frac{\rm cm^{-2}}{\rm K\ km\ s^{-1}}}\right)\left(\frac{1}{1+z}\right) \times\left(\frac{S_{\rm CO}\Delta\nu}{\rm Jy\ km\ s^{-1}}\right)\left(\frac{D_{\rm L}}{\rm Mpc}\right)^{2} M_{\odot}, \quad (7)$$

where $S_{\rm CO}\Delta\nu$ is the flux density expressed in Jy km s^{-1}, $D_{\rm L}$ is the luminosity distance in Mpc, and z is the redshift of the galaxy. Here we have assumed the Galactic CO-to-H_2 conversion factor $X_{\rm CO} = 2\times10^{20}$ cm^{-2} (K km s^{-1})$^{-1}$ and a constant CO (2–1)/CO (1–0) flux density ratio of 3.2 to convert CO (2–1) flux densities into estimated CO (1–0) values. The measured molecular gas mass values and upper limits are given in Table 3. Our derived cold gas masses are consistent with Boizelle et al. (2017) measurements.

Besides five ALMA molecular gas mass measurements, we also use previously published results of Young et al. (2011), Su & Irwin (2013), Boizelle et al. (2017), and Pulido et al. (2018) that have been obtained for galaxies related to the ATLAS^{3D} survey, individual ETGs, and galaxy clusters, including their BCGs. The ATLAS^{3D} survey is a volume-limited sample of 260 ETGs that is widely used to study ETG formation and evolution. This sample was observed in CO J = 1–0 and 2–1 using the IRAM 30 m telescope (Young et al. 2011), and 65% of them were observed in H I using the Westerbork Synthesis Radio Telescope (Morganti et al. 2006; Serra et al. 2012). CO emission was detected in 56 targets ($\sim$22%). Here we use 33 CO detections and upper limits of the ATLAS^{3D} survey. The clusters and their BCGs in Pulido et al. (2018) were observed in CO using the IRAM telescope as well.

5.2. $M_{\rm mol}$–$M_{\rm X}$ Relation

We plot molecular gas mass versus X-ray atmospheric gas mass in Figure 4. X-ray masses are derived within 10 kpc. This radius was chosen for two reasons. First, we wish to obtain a representative mass for the central galaxy that avoids the uncertainties associated with effective radius measurements. Second, thermodynamic parameters for cluster atmospheres, such as cooling time and entropy, have been reported at this radius to avoid resolution biases when comparing distant to nearby clusters (Rafferty et al. 2008). While this is not an issue for the ETGs studied here, it often is when comparing them to their distant cluster counterparts. In the nearest galaxies we have the opposite issue. Gas mass profiles extend out to only a few kiloparsecs before falling off the ACIS camera. In these instances, we have extrapolated their profiles using the linear slope of the last 5 points in log-log space. The BCGs represented as black circles in Figure 4 are taken from Pulido et al. (2018). The remaining points refer to the ETGs analyzed here. The morphological type of each galaxy is indicated: blue circles correspond to ellipticals, magenta circles correspond to S0/lenticular galaxies, and the yellow circles represent early spirals. Galaxies with recognizable disks are plotted with large shaded diamonds surrounding their native symbol.

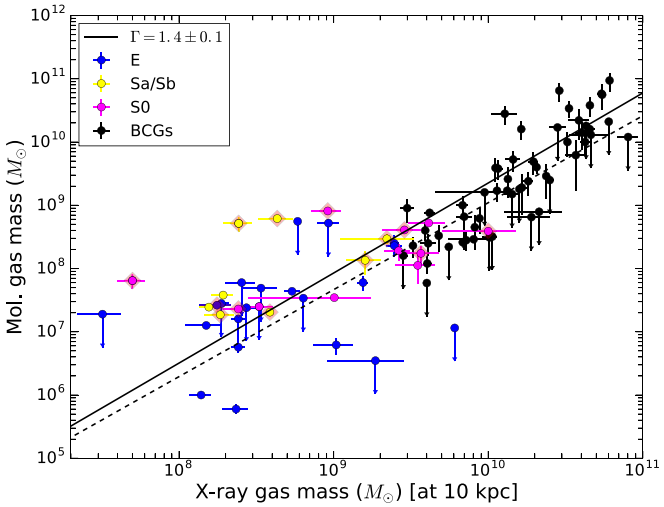

Figure 4. Relation of cold molecular gas mass to X-ray gas mass. The morphological type of each galaxy is indicated: blue circles correspond to ellipticals, magenta circles correspond to S0/lenticular galaxies, and yellow circles represent early spirals. Galaxies with recognizable disks are plotted with large shaded diamonds surrounding their native symbol.

Accounting for both detections and upper limits, a trend between molecular gas mass and atmospheric mass is found with correlation coefficient 0.76. The coefficient rises to 0.87 when the disk-like objects are excluded. The cold gas masses of galaxies with disks, $\sim10^7$–10^9 $M_\odot$, lie an order of magnitude above those without a clear disk, $\sim10^6$–10^8 $M_\odot$.

Figure 4 clearly shows an increase in scatter about the mean relationship in the lower-mass ETGs compared to the BCGs. While much is likely real mass variance, other factors may contribute, the most important being variance in the CO optical depth (Crocker et al. 2012). CO optical depth depends on the gas metallicity and the dynamical state of the gas (Alatalo et al. 2013). Different studies have also adopted different Galactic CO-to-H_2 conversion factors from those used in Pulido et al. (2018), Boizelle et al. (2017), and Young et al. (2011) depending on perceived conditions in the gas. However, these differences are generally a factor of a few or so, while the molecular gas mass at a given X-ray atmospheric gas mass in Figure 4 spans more than two orders of magnitude. Therefore, most of the scatter in the relationship is intrinsic.

A linear fit to the $M_{\rm mol}$–$M_{\rm X}$ relation was performed using only detections of cold gas masses. A bivariate correlated error and intrinsic scatter (BCES) routine (Akritas & Bershady 1996) was used to perform linear modeling in log space. Parameter errors are determined using 10,000 iterations of Monte Carlo

bootstrap resampling. Using the BCES routine, we found $M_{\rm mol} \propto M_{\rm X}^{1.4\pm0.1}$.

The best fit is shown in Figure 4 as a black solid line. Although a clear dependence of $M_{\rm mol}$ on $M_{\rm X}$ is found for clusters (BCGs), little correlation is found for the ETGs alone. Furthermore, the scatter about the mean of the ETGs exceeds that of the BCGs by a factor of 2. The relation between cold gas mass and X-ray mass for clusters alone follows the steeper form, $M_{\rm mol} \propto M_{\rm X}^{1.6\pm0.1}$. To explore this relationship further, we include the molecular mass upper limits using survival analysis.

5.2.1. Survival Analysis

Survival analysis is a powerful tool to estimate the likelihood and form of a relationship by evaluating both detections and upper limits (Feigelson & Nelson 1985; Isobe et al. 1986; Schmitt 1985). The likelihood is expressed as

$$L = \prod_{i=1}^{n} \mathrm{Prob}\left[t_i,\, \delta_i\right] = \prod_{i=1}^{n} \left[f(t_i)^{\delta_i}\right]\left[1 - S(t_i)\right]^{1-\delta_i}, \qquad (8)$$

where $t_i = \min(x_i,\, c_i)$, x_i are the detected values, c_i are the upper limits, and δ_i is 0 for upper limits and 1 for detections. The f_i and S_i are the likelihoods for detections and upper limits, respectively. In the case of normal (Gauss) distribution, the likelihood for the detected values can be expressed as

$$f(x) = \frac{1}{\sqrt{2\pi}\,\sigma} \exp\left[-\frac{1}{2}\left(\frac{x-\mu}{\sigma}\right)^2\right], \qquad (9)$$

where x and σ are the detected values of molecular gas mass and their errors, while μ is an assumed model of fitting. The likelihood for upper limits, $S(x)$, can be expressed as

$$S(x) = 1 - \frac{1}{2}\left[1 + \mathrm{erf}\left(\frac{x-\mu}{\sqrt{2}\,\sigma}\right)\right], \qquad (10)$$

where erf is the error function, $\mathrm{erf}(x) = \frac{2}{\sqrt{\pi}} \int_0^x e^{-t^2} dt$. In the case of Equation (10) we use $x = (\text{upper limit})_i$ and $\sigma = (\text{upper limit})_i/3$. We assume σ as $(\text{upper limit})_i/3$ since our upper limits were defined for the 3σ confidence level.

For the model, μ, we use the power law of the form of $A \times \left(\frac{x}{x_0}\right)^{\alpha}$. We find a slightly shallower relation, $M_{\rm mol} \propto M_{\rm X}^{1.37\pm0.21}$, than those obtained with the BCES routine that included only detections. The fit is presented in Figure 4 as a dashed line. Galaxies with gas disks have the largest residuals. Two disk systems are shown in Figure 5. Avoiding these points, the $M_{\rm mol}$–$M_{\rm X}$ relation follows a steeper relation with less scatter, $M_{\rm mol} \propto M_{\rm X}^{1.48\pm0.15}$.

Fits were calculated separately for the ETGs and cluster central galaxies. Including cluster central galaxies alone, we find $M_{\rm mol} \propto M_{\rm X}^{1.51\pm0.13}$. For ETGs we find $M_{\rm mol} \propto M_{\rm X}^{0.48\pm0.81}$. The ETGs alone reveal no correlation, implying two possibilities: either the molecular gas in ETGs is unrelated to atmospheric gas, or the range of molecular gas mass and atmospheric mass in the ETG sample is too limited relative to the variance to reveal the true underlying relationship. Statistics alone will not discriminate between these possibilities. However, other factors argue in favor of a physical trend from centrals in clusters to ETGs.

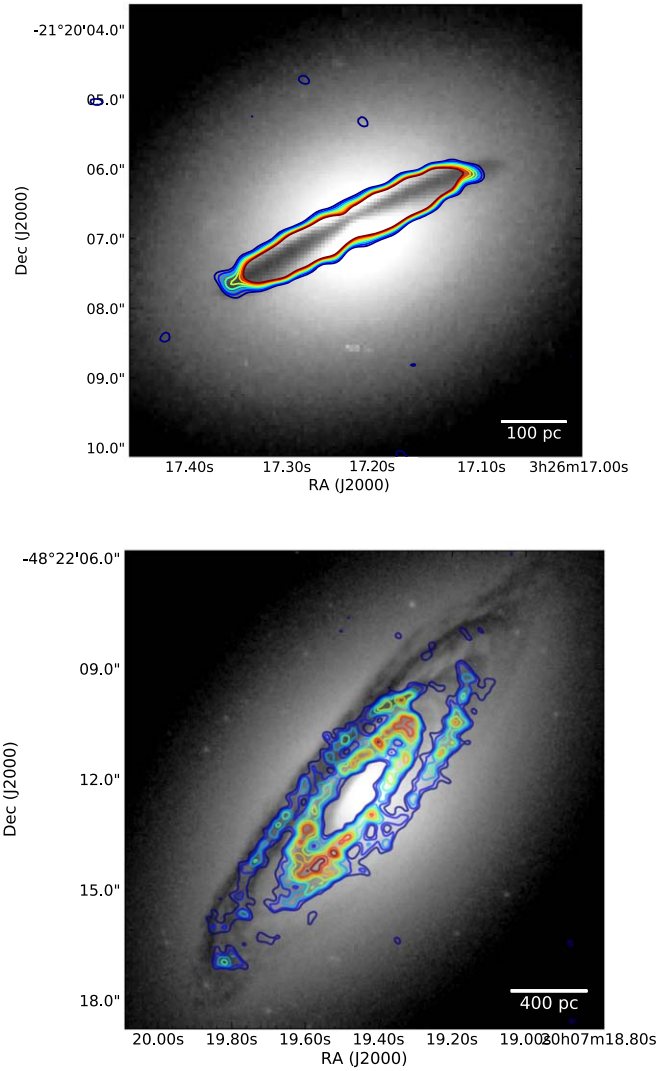

Figure 5. *HST* (F814W) linear grayscale images of NGC 1332 (top) and NGC 6861 (bottom) overlaid with ALMA CO (2–1) emission line contours from integrated intensity maps. In both images, contours start at the 3σ level and increase linearly.

First, molecular gas-rich galaxies all have similarly short atmospheric cooling times lying below 1 Gyr at 10 kpc (see below), while gas-poor systems have atmospheric cooling times exceeding 1 Gyr at 10 kpc. This is true in both ETGs and cluster centrals, where molecular gas masses are too high to have arrived in mergers.

Second, the ratio between atmospheric gas mass and molecular gas mass of the two populations is similar. Figure 6 shows the mass ratios of molecular to atmospheric gas for both cluster centrals and ETGs within a 10 kpc radius, where most molecular gas lies. This ratio lies between 10% and 20% on average but with large variance. The distribution of upper limits is broadly consistent with the detections, indicating that they are likely within factors of several of their true values.

This level of concordance would be difficult to understand if the origins of molecular clouds in BCGs and ETGs were dramatically different. For example, if the cold gas arrived exclusively by mergers or filaments, there is no obvious reason the atmospheric mass would exceed the molecular gas masses by such a large factor. Nevertheless, this figure indicates that

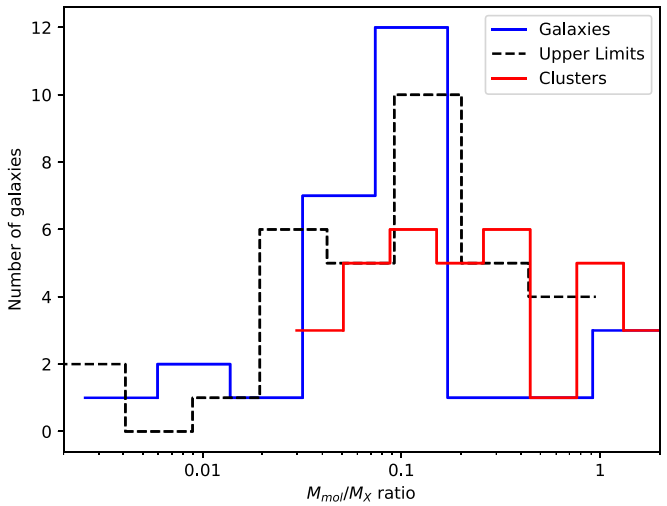

Figure 6. Fraction of molecular gas mass in X-ray gas mass for both high- and low-mass systems. The X-ray gas mass is taken at 10 kpc.

additional CO measurements are needed to convert the upper limits into detections before drawing firm conclusions about the relationships between cold gas and atmospheric cooling in ETGs.

5.3. Density, Temperature, and Luminosity

The dependence of molecular gas mass on atmospheric temperature, electron density, entropy, luminosity, and the minimum value of the t_c/t_{ff} ratio is investigated here. The top panel of Figure 7 shows molecular gas mass versus mean atmospheric gas temperature. The trend indicates that higher-temperature systems generally host more massive reservoirs of cold gas. This trend is not surprising, as it indicates that hotter, and hence more massive, systems attract and retain more massive molecular gas reservoirs. The scatter in molecular gas mass at a given temperature spans roughly two decades, indicating that mass alone does not determine the level of the molecular gas reservoir.

An indication that atmospheric gas density is a significant factor is shown in the bottom panel of Figure 7. The figure shows a trend between molecular gas mass and atmospheric gas density measured at an altitude of 10 kpc. This trend was found by Pulido et al. (2018) for cluster central galaxies. Their data are plotted to the upper right in Figure 7. The trend extends to ETGs, plotted to the lower left, albeit with greater scatter than the cluster central galaxies. It is not clear whether the greater scatter is intrinsic or due to the large number of upper limits.

A linear fit to the M_{mol}–n_e relation was performed using survival statistics. We find that this relation follows a power-law scaling as $M_{mol} \propto n_e^{1.8\pm0.2}$. The scatter of the M_{mol}–n_e relation is 0.34 dex, while the correlation coefficient is 0.86. The fit is shown as a dashed line in Figure 7. Separate analyses were performed for the clusters and ETGs alone. The cluster central (black points) relation follows a power-law scaling as $M_{mol} \propto n_e^{2.2\pm0.4}$. This is slightly steeper compared to the full M_{mol}–n_e relation. However, both are consistent within their uncertainties. In the case of low-mass systems (blue, magenta, and yellow points), we find $M_{mol} \propto n_e^{1.5\pm1.1}$, which is shallower than both the entire sample and cluster central galaxies alone. However, the slope of the M_{mol}–n_e relation for ETGs is

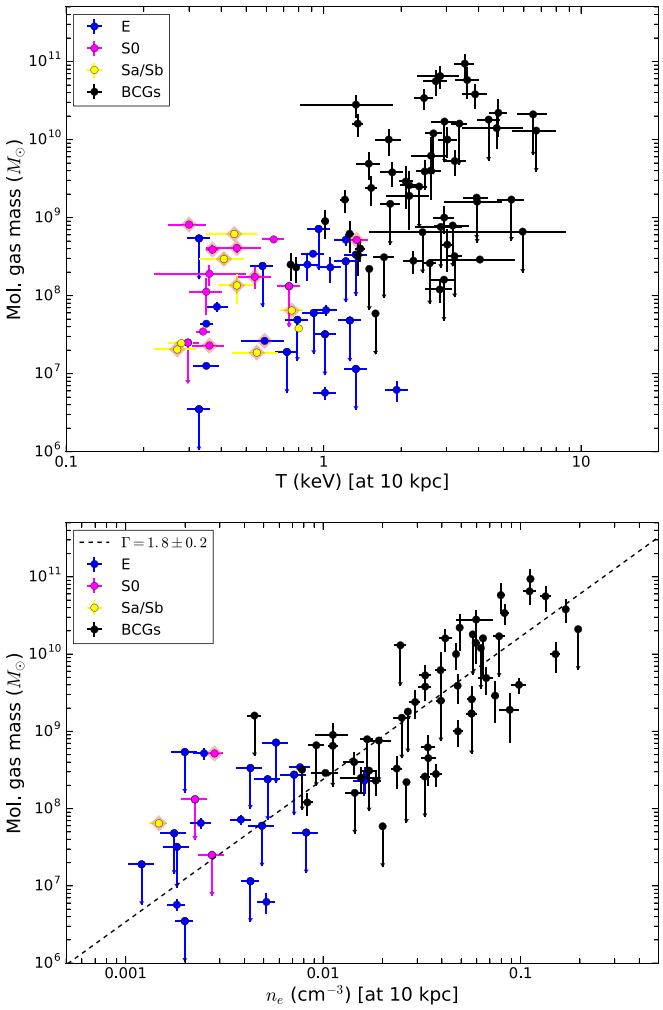

Figure 7. Molecular gas mass vs. temperature (top panel) and electron density at 10 kpc (bottom panel). The M_{mol}–T relation includes the spectral temperature measurements presented in Table 2.

consistent, within uncertainties, with the full sample. The scatter of the M_{mol}–n_e relation for BCGs is 0.24 dex, while for low-mass systems it is 0.56 dex.

The M_{mol}–L_X relation for the entire sample was constructed. The X-ray luminosity within 10 kpc was computed as $L_X = 4\pi D_L^2 f_X$, where f_X is the X-ray flux obtained from spectral fitting. The M_{mol}–L_X relation is shown in Figure 8. The survival fit for the entire sample yields $M_{mol} \propto L_X^{1.3\pm0.2}$. The scatter is only 0.25 dex, demonstrating a tight dependence. The separate fits for the ETGs and cluster central galaxies alone yield $M_{mol} \propto L_X^{0.5\pm0.8}$ and $M_{mol} \propto L_X^{1.2\pm0.1}$, respectively. Therefore, the trends are consistent with each other, albeit with large scatter in the ETGs. The M_{mol}–L_X relation for ETGs alone is consistent with O'Sullivan et al. (2018), who likewise found no clear correlation between CO emission and the absence or presence of a hot intragroup medium.

5.4. Discussion

5.4.1. Does Molecular Gas Fuel Radio/AGN Feedback?

Maintaining balance between heating and cooling of hot atmospheres across a large range of halo mass requires a reliable fuel supply to the AGN. Bondi accretion of the hot atmosphere onto the central black hole would be a feasible fuel

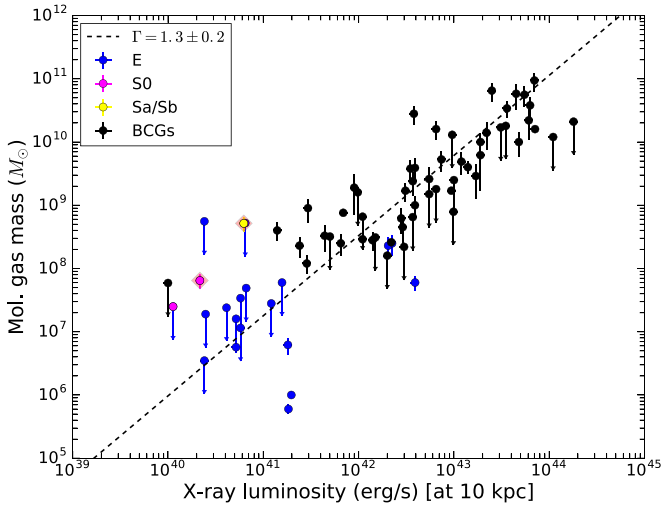

Figure 8. Molecular gas mass vs. X-ray luminosity defined at 10 kpc. The $M_{\rm mol}$–$L_{\rm X}$ relation is fitted by a power-law model using survival analysis.

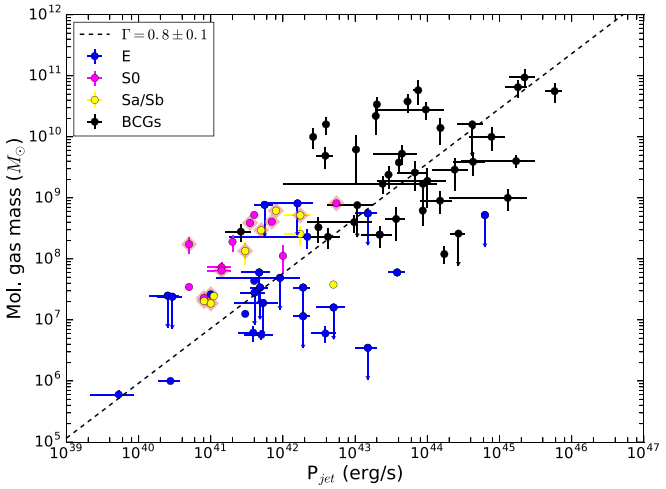

Figure 9. Relation of cold molecular gas mass vs. AGN jet power. The dashed line corresponds to the survival fitting.

supply in ETGs (Allen et al. 2006; Hardcastle et al. 2006; Rafferty et al. 2006; Narayan & Fabian 2011). However, Bondi accretion would be unable to fuel the most powerful AGN (Russell et al. 2013) in cluster central galaxies (Hardcastle et al. 2006; Rafferty et al. 2006; McNamara et al. 2011). The CO detections and upper limits in cluster central galaxies and ETGs are easily sufficient to fuel radio AGNs. But no trend between molecular gas and radio AGN power has been found.

Using a recent X-ray cavity analysis, we adopt the scaling relation between radio power and AGN jet power (Cavagnolo et al. 2010) to explore this trend. Radio power was calculated using the relation

$$P_{\nu_0} = 4\pi D_{\rm L}^2 (1+z)^{\alpha-1} S_{\nu_0} \nu_0, \quad (11)$$

where S_{ν_0} is the flux density at the observed frequency ν_0, z is the redshift, $D_{\rm L}$ is the luminosity distance, and α is the radio spectral index. The radio flux densities, S_{ν_0}, were taken from the NRAO VLA Sky Survey (NVSS; Condon et al. 1998). We found no radio fluxes for 22 galaxy clusters. We assume spectral index $\alpha = 0.8$ and $\nu_0 = 1.4$ GHz. We estimate the AGN mechanical power in BCGs to be 10^{43}–10^{45} erg s^{-1}, which is two to three orders of magnitude higher than those in the ETG sample.

The correlation between molecular gas mass and radio jet power is presented in Figure 9. A weak trend over five decades in molecular gas mass and nearly six decades in jet power is found. The scaling is nearly linear, following $M_{\rm mol} \propto P_{\rm jet}^{0.8\pm0.1}$ with a standard deviation of 1.21 dex. However, the correlation coefficient 0.64 indicates that the trend is at best marginally significant. For a given molecular gas mass, one finds roughly three decades of variation in jet power, and conversely so. A similar variance was noted by McNamara et al. (2011) in cluster central galaxies alone.

To further evaluate the degree of correlation between these quantities, we explore the influence of the D^2 factor on both axes. We generated random redshift, distance, and flux data sets with the correct spread given by error bars over the observed range. We recovered the scatter in the observed $M_{\rm mol}$–$P_{\rm jet}$ relation, but the simulated slope, 1.0 ± 0.03, was steeper than the observed slope 0.8 ± 0.1, at about the 2σ significance level. This result is consistent with the correlation coefficient, which indicated only marginal significance.

One would naively expect a large scatter and hence a weak correlation between jet power and the level of the molecular gas reservoir. Only a tiny fraction of the molecular gas reservoirs shown in Figure 9 would be required to fuel the AGN at the levels observed in this figure (McNamara et al. 2011). Furthermore, the molecular gas is distributed on much larger scales than the central black hole's sphere of influence. Thus, the timescale for most of the molecular gas to accrete onto the central black hole dramatically exceeds the age of the AGN. Only the mass on small scales is currently participating in fueling the AGN. Therefore, the trend indicates that systems that on average have higher AGN jet power also contain larger molecular gas reservoirs available to fuel the AGN.

Correlations between jet power, atmospheric gas mass within 10 kpc, total mass within 10 kpc, and total mass within R_{2500} are explored in Figure 10. Weak correlations are found between AGN jet power and both atmospheric gas mass (correlation coefficient 0.48) and total mass, M_{2500} (correlation coefficient 0.44). M_{2500} for the ETGs was determined using the M_{2500}–T scaling relation of Vikhlinin et al. (2006). This approach was adopted because we are unable to trace the gas density and temperature out to this distance for the nearest galaxies. In contrast, cluster central masses, M_{2500}, can be measured directly (Hogan et al. 2017b; Pulido et al. 2018). The extrapolation to R_{2500} contributes scatter to the ETG measurements. However, a correlation between molecular gas mass and total mass within R_{2500} is apparent. In contrast, no correlation is found between AGN jet power and total mass within 10 kpc. The absence of correlation is likely due to the dominant stellar component in the total mass within 10 kpc, which would not participate in fueling the AGN. It is interesting, nevertheless, that M_{2500} and the atmospheric gas are correlated with AGN jet power.

These trends are consistent with the large-scale mass dependence of AGN power in systems with central cooling times shorter than 1 Gyr (Main et al. 2017) in clusters. This new result extends Main's to ETGs. This correlation indicates that AGN power, which emerges from processes near to the event horizon, is regulated by conditions on vastly larger scales.

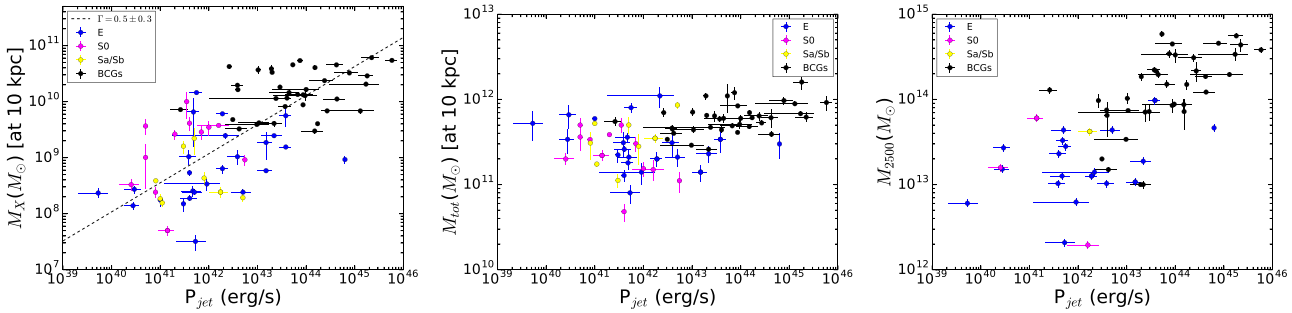

Figure 10. X-ray gas mass, total mass, and M_{2500} vs. the radio AGN jet power (from left to right).

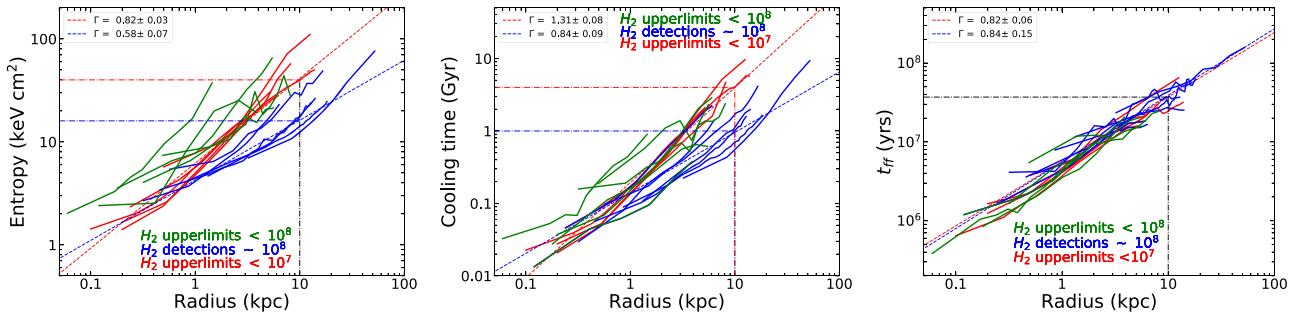

Figure 11. Entropy, cooling, and free-fall time profiles of low-mass systems with/without evidence of CO detection and H_2 gas. The systems, shown in blue, are detected with CO masses exceeding $10^8\,M_\odot$, while shown in red and green are upper limit detections with CO masses below 10^7 and 10^8, respectively. Red and blue power-law fits (dashed lines) are performed using the BCES routine. Dashed–dotted lines correspond to the crossing between the best-fitting lines with observations at 10 kpc.

5.4.2. Cold Gas in Early-type Galaxies

While the origin of molecular gas in BCGs is almost certainly cooling from the hot atmosphere, its origin in ETGs is less clear. Internal origins include stellar ejecta and atmospheric cooling, or externally accreted gas from mergers of gas-rich galaxies. We discuss these ideas in turn.

5.5. Atmospheric Cooling

Using the *Herschel Space Observatory*, Werner et al. (2014) showed that the molecular cooling lines of [C II] and [O I] correlate with nebular emission in some ETGs. The systems with nebular emission demonstrate flatter entropy profiles than those without nebular emission, tentatively connecting the cold gas to cooling from the hot atmospheres. They also found that thermally unstable systems indicated by the "Field Criterion" are likely to have [C II] emission from warm molecular gas. This again is consistent with cooling from the hot atmosphere. Similar results have been found in cluster BCG atmospheres (Cavagnolo et al. 2008; Rafferty et al. 2008; Voit et al. 2008).

The Werner et al. (2014) study was extended to 49 nearby elliptical galaxies by Lakhchaura et al. (2018), who found a similar connection between nebular emission and cooling hot atmospheres, indicating a common origin between the hot atmosphere and molecular gas. Lakhchaura's sample significantly overlaps our own. The correlations we find here between the thermodynamic properties of hot atmospheres and CO mass, in combination with the Werner and Lakhchaura results, point to cooling from hot atmospheres as a significant, perhaps the most significant, source of molecular gas in ETGs.

The presence or absence of a significant molecular gas signal in cluster central galaxies is closely tied to cooling time. Systems with atmospheric cooling times at roughly 10 kpc in altitude that lie below $\sim 10^9$ yr are likely to be detected (Pulido et al. 2018). Those with longer cooling times are not. A similar trend is found using the entropy parameter. This condition is tested in ETGs in Figure 11. This figure shows that systems with shallower entropy profiles and lower entropy at 10 kpc, shown in blue, are detected with CO masses exceeding $10^8\,M_\odot$. Their entropies at 10 kpc are in the range of 10–30 keV cm^2, consistent with central galaxies in clusters that are rich in molecular gas. Objects with restrictive CO upper limits that lie at or below $10^7\,M_\odot$, shown in red, have entropies lying above 40 keV cm^2. Systems with less restrictive upper limits that lie below $10^8\,M_\odot$, shown in green, have similarly high entropy. The entropy profiles presented here are consistent with Werner et al. (2014).

The middle panel of Figure 11 shows a similar trend in atmospheric cooling time. Systems with atmospheric cooling time at 10 kpc that lie below ~1 Gyr are detected in CO. This segregation continues inward to approximately 1 kpc, where all profiles merge. This merging could be real, or it may be the consequence of our inability to resolve the gas temperature in the inner bins (see Hogan et al. 2017a, for detailed discussion). In fact, there is nothing special about 10 kpc. It is approximately the radius at which the cooling time and entropy parameters can be resolved in cluster centrals. Presumably in those systems, like these, the profiles remain segregated as they move inward. Nevertheless, the profiles show that the atmospheric cooling time in systems with significant molecular gas lies below that in systems without molecular gas over most of the volume within 10 kpc. Like cluster centrals with large molecular gas masses, short cooling times in the atmospheres of normal ellipticals apparently correlate with significant levels of molecular gas.

Free-fall time profiles are shown in the right panel. All are similar and reveal little scatter at 10 kpc. Nevertheless, dividing the cooling time and free-fall time profiles only scatters the

trend in Figure 3. The free-fall time adds no leverage; the t_c/t_{ff} ratio plays no obvious role. While the sample is admittedly small, this diagram shows that t_c is an effective indicator for the presence of cold molecular gas. Similar trends are found in cluster central galaxies (Hogan et al. 2017b; Pulido et al. 2018; Babyk et al. 2018b). This result implicates the hot atmosphere in the production of molecular clouds in ETGs, presumably through cooling.

Finally, three systems in Figure 4 have elevated levels of molecular gas relative to their atmospheric masses. All three are early spirals, and their gas lies in rotating disks. Molecular disks are often attributed to high angular momentum mergers, and this may be true. However, an internal atmospheric origin cannot be ruled out.

Werner et al. (2014) and Negri et al. (2014) pointed out that thermally unstable cooling may be enhanced in rotating atmospheres. Rotation reduces the effective gravity and thus prevents a thermally unstable parcel of gas from sinking to its equilibrium position. This would lead to unstable cooling on nonradial orbits. If the cooling gas is unable to shed its angular momentum, it would settle into a molecular disk (see also Sobacchi & Sormani 2019). Molecular clouds are observed preferentially in fast-rotating ETGs (Davis et al. 2019). If the atmospheres and stars are corotating, thermally unstable cooling may be enhanced, leading to the observed correlation.

5.6. Merger Origin

Molecular and atomic gas clouds in ETGs are commonly attributed to mergers. Davis et al. (2011) compared the angular momentum vectors of the cold gas and stars in ATLAS^{3D} galaxies and attributed their misalignments to oblique-angle mergers. These studies and others (Young 2002; Young et al. 2008; Crocker et al. 2011) have argued that cold clouds forming from debris lost from stars should share the stellar angular momentum vector. Misaligned vectors would indicate an external origin.

Using a simple model prescription incorporating a variety of physical processes including mergers and feedback, Davis et al. (2019) estimated the gas-rich merger rate of ellipticals in the local universe. They concluded that mergers are likely the primary source of cold gas in ETGs. In their model, atmospheric cooling, stellar mass loss, and other sources contribute less to the cold gas budget. Their conclusion is based in part on the absence of correlation between stellar mass and molecular clouds, as would be expected if cold clouds condensed from stellar ejecta.

Misaligned angular momenta need not in themselves imply an external origin for cold gas. Semianalytic models of galaxies evolving in a Lambda-CDM cosmology (Lagos et al. 2015) indicate that the high fraction of misaligned gas disks in the ATLAS^{3D} catalog may be caused by angular momentum misalignments between cooling hot atmospheres, stars, and dark matter halos. Their simulations further indicated that the frequency of mergers at the low redshifts found in the ATLAS^{3D} sample, ∼40%, is too low to account for the high incidence of cold gas, whose angular momentum is misaligned with the stars. In a related study, Lagos et al. (2014) concluded that most neutral gas (atomic + molecular) in nearby ETGs likely cooled from their hot atmospheres.

5.7. Stellar Ejecta

Spitzer and *Herschel* observations of ETGs reveal the presence of polycyclic aromatic hydrocarbon, warm and cold H2, and dust (see Werner et al. 2014, and references therein). The presence of polycyclic aromatic hydrocarbon and dust in the cold gas clouds indicates that some fraction of the cold gas originated from stellar mass loss (Werner et al. 2014). However, Goulding et al. (2016) showed that while the thermalization of stellar ejecta (mass loss, supernovae) is a significant source of atmospheric gas (see also Pellegrini et al. (2018), their data are inconsistent with a stellar mass-loss origin alone.

In summary, the origins of cold gas in ETGs are poorly understood. They may acquire their molecular clouds at some level by all three mechanisms. Occasional mergers would be an appealing mechanism to explain the scatter in the trends presented here. However, the trends themselves indicate that condensation from hot atmospheres is a significant source of cold gas in ETGs.

5.8. Neutral Hydrogen in Hot Atmospheres

This study is focused on molecular gas owing to the availability of CO measurements for large numbers of cluster centrals and nearby ETGs. Nevertheless, H I is crucial to the picture. Studies have shown that ETGs tend to be underabundant in H I compared to spirals (Young & Knezek 1989; Young & Scoville 1991; Sage 1993; Obreschkow 2008; Oosterloo et al. 2010). Although the variance is large, the relatively low average abundance of H I implies a rapid transition of cold atomic clouds to molecular clouds in hot atmospheres. This transition may be related to high atmospheric gas pressures found in giant ellipticals and cluster centrals.

Elmegreen (1993) showed that H I in diffuse interstellar clouds should transform rapidly into H2 when clouds are shielded from strong ultraviolet radiation and experience high ambient pressure. Assuming that diffuse, nongravitating clouds have an internal density that scales with ambient pressure, the clouds will quickly transform their H I into H2. Blitz & Rosolowsky (2004, 2006) examined this conjecture in a sample of nearby disk galaxies. They found that the ratio of atomic to molecular gas rises from well below unity to nearly 100 as the external pressure rises from $\sim 10^4$ to $\sim 10^6$ cm^3 K. This trend correlates almost linearly with ambient pressure.

Atmospheres are volume-filling, so they are likely to be in pressure contact with molecular clouds. The atmospheric pressures observed in this sample would place them on the high end of the Blitz–Rosolowsky correlation, consistent with the relatively low abundance of H I in these systems. This issue will be explored in a future work.

6. Conclusions

The thermodynamic properties of the hot atmospheres and molecular gas content of 40 ETGs observed with *Chandra* and the ATLAS^{3D} project were analyzed. Their properties were compared to those of central cluster galaxies rich in molecular gas. Our conclusions are summarized as follows:

(i) Molecular gas mass is correlated with atmospheric gas mass, atmospheric density, and atmospheric X-ray luminosity over five decades in molecular gas mass,

from ETGs to central cluster galaxies. The most distant outliers are early-type disk galaxies, which have higher levels of molecular gas compared to those without molecular disks.

(ii) The ratio of cold molecular gas to hot atmospheric gas within 10 kpc of the galaxy is similar over a broad range in halo mass, from giant ellipticals to central cluster galaxies, and lies between 10% and 20%.

(iii) Molecular gas in ETGs is found preferentially in systems when the cooling time of their hot atmosphere lies below $\sim 10^9$ yr at an altitude of 10 kpc. This "cooling time threshold" is similar to what is found in cluster central galaxies.

This study indicates a relationship between the molecular gas content of ETGs and their hot atmospheres. The apparent continuity between the molecular gas content and atmospheric properties of cluster central galaxies, which are almost certainly due to cooling, likewise suggests that some or most of the molecular gas in ETGs cooled from their atmospheres. Taking different approaches, Werner et al. (2014) and Lakhchaura et al. (2018) reached similar conclusions.

Nevertheless, the connection between hot atmospheres and molecular gas in ETGs is not as strong as it is for central galaxies in clusters. This is largely due to lower gas masses and poorer detection statistics. Additional data from ALMA and other cold gas tracers are needed to further explore this conjecture.

B.R.M. acknowledges support from the Natural Sciences and Engineering Research Council of Canada. H.R.R. acknowledges support from an STFC Ernest Rutherford Fellowship. A.C.E. acknowledges support from STFC grant ST/P00541/1. B.R.M. thanks Leo Blitz for an insightful discussion during a visit to the Flatiron Institute. We thank the referee for comments that significantly improved the paper. The scientific results reported in this article are based on observations made by the *Chandra X-ray Observatory* and have made use of software provided by the Chandra X-ray Center (CXC) in the application packages CIAO, ChIPS, and Sherpa. This paper makes use of the following ALMA data: #2013.1.00229.S, #2015.1.00989.S, #2015.1.01198.S, and #2015.1.01572.S. ALMA is a partnership of ESO (representing its member states), NSF (USA), and NINS (Japan), together with NRC (Canada), MOST and ASIAA (Taiwan), and KASI (Republic of Korea), in cooperation with the Republic of Chile. The Joint ALMA Observatory is operated by ESO, AUI/NRAO, and NAOJ.

ORCID iDs

Iu. V. Babyk https://orcid.org/0000-0003-3165-9804
B. R. McNamara https://orcid.org/0000-0002-2622-2627
P. E. J. Nulsen https://orcid.org/0000-0003-0297-4493
A. C. Edge https://orcid.org/0000-0002-3398-6916

References

Akritas, M. G., & Bershady, M. A. 1996, ApJ, 470, 706
Alatalo, K., Davis, T. A., Bureau, M., et al. 2013, MNRAS, 432, 1796
Allen, S. W., Dunn, R. J. H., Fabian, A. C., Taylor, G. B., & Reynolds, C. S. 2006, MNRAS, 372, 21
Arnaud, K. A. 1996, in ASP Conf. Ser. 101, Astronomical Data Analysis Software and Systems V, ed. G. H. Jacoby & J. Barnes (San Francisco, CA: ASP), 17
Babyk, I. 2012, JPhSt, 16, 1904
Babyk, I. 2016, ARep, 60, 542
Babyk, I., & Del Popolo, A. 2014, BaltA, 23, 9
Babyk, I. V., McNamara, B. R., Nulsen, P. E. J., et al. 2018a, ApJ, 857, 32
Babyk, I. V., McNamara, B. R., Nulsen, P. E. J., et al. 2018b, ApJ, 862, 39
Babyk, I. V., & Vavilova, I. B. 2012, OAP, 25, 119
Babyk, I. V., & Vavilova, I. B. 2013, OAP, 26, 175
Babyk, Y. V., Del Popolo, A., & Vavilova, I. B. 2014, ARep, 58, 587
Blitz, L., & Rosolowsky, E. 2004, ApJL, 612, L29
Blitz, L., & Rosolowsky, E. 2006, ApJ, 650, 933
Boizelle, B. D., Barth, A. J., Darling, J., et al. 2017, ApJ, 845, 170
Bolatto, A. D., Wolfire, M., & Leroy, A. K. 2013, ARA&A, 51, 207
Boroson, B., Kim, D.-W., & Fabbiano, G. 2011, ApJ, 729, 12
Cappellari, M., Emsellem, E., Krajnovic, D., et al. 2011, MNRAS, 413, 813
Cavagnolo, K. W., Donahue, M., Voit, G. M., & Sun, M. 2008, ApJL, 683, L107
Cavagnolo, K. W., McNamara, B. R., Nulsen, P. E. J., et al. 2010, ApJ, 720, 1066
Cavaliere, A., & Fusco-Femiano, R. 1978, A&A, 70, 677
Choudhury, P. P., & Sharma, P. 2016, MNRAS, 457, 2554
Combes, F., Young, L. M., & Bureau, M. 2007, MNRAS, 377, 1795
Condon, J. J., Cotton, W. D., Greisen, E. W., et al. 1998, AJ, 115, 1693
Crawford, C. S., Allen, S. W., Ebeling, H., Edge, A. C., & Fabian, A. C. 1999, MNRAS, 306, 857
Crocker, A., Krips, M., Bureau, M., et al. 2012, MNRAS, 421, 1298
Crocker, A. F., Bureau, M., Young, L. M., & Combes, F. 2011, MNRAS, 410, 1197
David, L. P., Lim, J., Forman, W., et al. 2014, ApJ, 792, 94
David, L. P., Vrtilek, J., O'Sullivan, E., et al. 2017, ApJ, 842, 84
Davis, T. A., Alatalo, K., Sarzi, M., et al. 2011, MNRAS, 417, 882
Davis, T. A., Greene, J. E., Ma, C.-P., et al. 2019, MNRAS, 486, 1404
Dickey, J. M., & Lockman, F. J. 1990, ARA&A, 28, 215
Draine, B. T., & Salpeter, E. E. 1979, ApJ, 231, 438
Edge, A. C. 2001, MNRAS, 328, 762
Edge, A. C., Wilman, R. J., Johnstone, R. M., et al. 2002, MNRAS, 337, 49
Elmegreen, B. G. 1993, ApJ, 411, 170
Emsellem, E., Cappellari, M., Krajnović, D., et al. 2011, MNRAS, 414, 888
Emsellem, E., Greusard, D., Combes, F., et al. 2001, A&A, 368, 52
Fabian, A. C., Celotti, A., Blundell, K. M., Kassim, N. E., & Perley, R. A. 2002, MNRAS, 331, 369
Fabian, A. C., Sanders, J. S., Allen, S. W., et al. 2003, MNRAS, 344, L43
Feigelson, E. D., & Nelson, P. I. 1985, ApJ, 293, 192
Forbes, D. A., Alabi, A., Romanowsky, A. J., et al. 2017, MNRAS, 464, L26
Ford, H. A., & Bregman, J. N. 2013, ApJ, 770, 137
Forman, W., Jones, C., & Tucker, W. 1985, ApJ, 293, 102
Fruscione, A., McDowell, J. C., Allen, G. E., et al. 2006, Proc. SPIE, 6270, 62701V
Gaspari, M., Brighenti, F., & Temi, P. 2012, MNRAS, 424, 190
Gaspari, M., & Churazov, E. 2013, A&A, 559, A78
Gitti, M., Nulsen, P. E. J., David, L. P., McNamara, B. R., & Wise, M. W. 2011, ApJ, 732, 13
Goudfrooij, P., de Jong, T., Hansen, L., & Norgaard-Nielsen, H. U. 1994, MNRAS, 271, 833
Goulding, A. D., Greene, J. E., Ma, C.-P., et al. 2016, ApJ, 826, 167
Griffith, E., Martini, P., & Conroy, C. 2019, MNRAS, 484, 562
Hardcastle, M. J., Evans, D. A., & Croston, J. H. 2006, MNRAS, 370, 1893
Hatch, N. A., Crawford, C. S., Johnstone, R. M., & Fabian, A. C. 2006, MNRAS, 367, 433
Heckman, T. M., Baum, S. A., van Breugel, W. J. M., & McCarthy, P. 1989, ApJ, 338, 48
Hlavacek-Larrondo, J., McDonald, M., Benson, B. A., et al. 2015, ApJ, 805, 35
Hogan, M. T., McNamara, B. R., Pulido, F., et al. 2017a, ApJ, 837, 51
Hogan, M. T., McNamara, B. R., Pulido, F. A., et al. 2017b, ApJ, 851, 66
Hu, E. M., Cowie, L. L., & Wang, Z. 1985, ApJS, 59, 447
Isobe, T., Feigelson, E. D., & Nelson, P. I. 1986, ApJ, 306, 490
Kaastra, J. S., & Mewe, R. 1993, A&AS, 97, 443
Kalberla, P. M. W., Burton, W. B., Hartmann, D., et al. 2005, A&A, 440, 775
Kim, D.-W., & Fabbiano, G. 2013, ApJ, 776, 116
Kim, D.-W., & Fabbiano, G. 2015, ApJ, 812, 127
Kirkpatrick, C. C., & McNamara, B. R. 2015, MNRAS, 452, 4361
Kormendy, J., & Ho, L. C. 2013, ARA&A, 51, 511
Lagos, C. d. P., Davis, T. A., Lacey, C. G., et al. 2014, MNRAS, 443, 1002
Lagos, C. d. P., Padilla, N. D., Davis, T. A., et al. 2015, MNRAS, 448, 1271

Lakhchaura, K., Werner, N., Sun, M., et al. 2018, MNRAS, 481, 4472
Le Bourlot, J., Le Petit, F., Pinto, C., Roueff, E., & Roy, F. 2012, A&A, 541, A76
Li, Y., & Bryan, G. L. 2014, ApJ, 789, 153
Li, Y., Bryan, G. L., Ruszkowski, M., et al. 2015, ApJ, 811, 73
Liedahl, D. A., Osterheld, A. L., & Goldstein, W. H. 1995, ApJL, 438, L115
Ma, C.-P., Greene, J. E., McConnell, N., et al. 2014, ApJ, 795, 158
Main, R. A., McNamara, B. R., Nulsen, P. E. J., Russell, H. R., & Vantyghem, A. N. 2017, MNRAS, 464, 4360
Mathews, W. G., & Brighenti, F. 2003, ARA&A, 41, 191
McCourt, M., Sharma, P., Quataert, E., & Parrish, I. J. 2012, MNRAS, 419, 3319
McDonald, M., Veilleux, S., Rupke, D. S. N., & Mushotzky, R. 2010, ApJ, 721, 1262
McNamara, B. R., & Jaffe, W. 1994, A&A, 281, 673
McNamara, B. R., Rohanizadegan, M., & Nulsen, P. E. J. 2011, ApJ, 727, 39
McNamara, B. R., Russell, H. R., Nulsen, P. E. J., et al. 2014, ApJ, 785, 44
McNamara, B. R., Russell, H. R., Nulsen, P. E. J., et al. 2016, ApJ, 830, 79
Mei, S., Blakeslee, J. P., Côté, P., et al. 2007, ApJ, 655, 144
Mewe, R., Lemen, J. R., & van den Oord, G. H. J. 1986, A&AS, 65, 511
Morganti, R., de Zeeuw, P. T., Oosterloo, T. A., et al. 2006, MNRAS, 371, 157
Narayan, R., & Fabian, A. C. 2011, MNRAS, 415, 3721
Navarro, J. F., Ludlow, A., Springel, V., et al. 2010, MNRAS, 402, 21
Negri, A., Posacki, S., Pellegrini, S., & Ciotti, L. 2014, MNRAS, 445, 1351
Nulsen, P. E. J. 1986, MNRAS, 221, 377
Obreschkow, D. 2008, in AIP Conf. Ser. 1035, The Evolution of Galaxies through the Neutral Hydrogen Window, ed. R. Minchin & E. Momjian (Melville, NY: AIP), 33
Oosterloo, T., Morganti, R., Crocker, A., et al. 2010, MNRAS, 409, 500
O'Sullivan, E., Combes, F., Salomé, P., et al. 2018, A&A, 618, A126
Pellegrini, S., Ciotti, L., Negri, A., & Ostriker, J. P. 2018, ApJ, 856, 115
Pizzolato, F., & Soker, N. 2005, ApJ, 632, 821
Pulatova, N. G., Vavilova, I. B., Sawangwit, U., Babyk, I., & Klimanov, S. 2015, MNRAS, 447, 2209
Pulido, F. A., McNamara, B. R., Edge, A. C., et al. 2018, ApJ, 853, 177
Rafferty, D. A., McNamara, B. R., & Nulsen, P. E. J. 2008, ApJ, 687, 899
Rafferty, D. A., McNamara, B. R., Nulsen, P. E. J., & Wise, M. W. 2006, ApJ, 652, 216
Revaz, Y., Combes, F., & Salomé, P. 2008, A&A, 477, L33
Russell, H. R., Fabian, A. C., McNamara, B. R., & Broderick, A. E. 2015, MNRAS, 451, 588
Russell, H. R., McDonald, M., McNamara, B. R., et al. 2017a, ApJ, 836, 130
Russell, H. R., McNamara, B. R., Edge, A. C., et al. 2013, MNRAS, 432, 530
Russell, H. R., McNamara, B. R., Edge, A. C., et al. 2014, ApJ, 784, 78
Russell, H. R., McNamara, B. R., Fabian, A. C., et al. 2016, MNRAS, 458, 3134
Russell, H. R., McNamara, B. R., Fabian, A. C., et al. 2017b, MNRAS, 472, 4024
Russell, H. R., McNamara, B. R., Fabian, A. C., et al. 2019, MNRAS, 490, 3025
Russell, H. R., Sanders, J. S., & Fabian, A. C. 2008, MNRAS, 390, 1207
Sadler, E. M., & Gerhard, O. E. 1985, MNRAS, 214, 177
Sage, L. J. 1993, A&A, 272, 123
Salomé, P., & Combes, F. 2003, A&A, 412, 657
Salomé, P., Combes, F., Revaz, Y., et al. 2011, A&A, 531, A85
Schmitt, J. H. M. M. 1985, ApJ, 293, 178
Serra, P., Oosterloo, T., Morganti, R., et al. 2012, MNRAS, 422, 1835
Shapiro, K. L., Falcón-Barroso, J., van de Ven, G., et al. 2010, MNRAS, 402, 2140
Sharma, P., McCourt, M., Quataert, E., & Parrish, I. J. 2012, MNRAS, 420, 3174
Simionescu, A., Tremblay, G., Werner, N., et al. 2018, MNRAS, 475, 3004
Simionescu, A., Werner, N., Forman, W. R., et al. 2010, MNRAS, 405, 91
Smith, G. P., Kneib, J.-P., Ebeling, H., Czoske, O., & Smail, I. 2001, ApJ, 552, 493
Sobacchi, E., & Sormani, M. C. 2019, MNRAS, 486, 205
Solomon, P. M., & Vanden Bout, P. A. 2005, ARA&A, 43, 677
Su, Y., & Irwin, J. A. 2013, ApJ, 766, 61
Tremblay, G. R., Oonk, J. B. R., Combes, F., et al. 2016, Natur, 534, 218
Trinchieri, G., & Fabbiano, G. 1985, ApJ, 296, 447
van Dokkum, P. G., & Franx, M. 1995, AJ, 110, 2027
Vantyghem, A. N., McNamara, B. R., Edge, A. C., et al. 2017, ApJ, 848, 101
Vantyghem, A. N., McNamara, B. R., Russell, H. R., et al. 2016, ApJ, 832, 148
Vantyghem, A. N., McNamara, B. R., Russell, H. R., et al. 2018, ApJ, 863, 193
Vavilova, I. B., Bolotin, Y. L., Boyarsky, A. M., et al. 2015, Dark Matter: Observational Manifestation and Experimental Searches (Kiev: Akademperiodyka)
Vikhlinin, A., Kravtsov, A., Forman, W., et al. 2006, ApJ, 640, 691
Voit, G. M., Babul, A., Babyk, I., et al. 2019, BAAS, 51, 405
Voit, G. M., Cavagnolo, K. W., Donahue, M., et al. 2008, ApJL, 681, L5
Voit, G. M., & Donahue, M. 2015, ApJL, 799, L1
Voit, G. M., Donahue, M., O'Shea, B. W., et al. 2015, ApJL, 803, L21
Werner, N., Allen, S. W., & Simionescu, A. 2012, MNRAS, 425, 2731
Werner, N., McNamara, B. R., Churazov, E., & Scannapieco, E. 2019, SSRv, 215, 5
Werner, N., Oonk, J. B. R., Sun, M., et al. 2014, MNRAS, 439, 2291
Werner, N., Urban, O., Simionescu, A., & Allen, S. W. 2013, Natur, 502, 656
Wong, K.-W., Irwin, J. A., Shcherbakov, R. V., et al. 2014, ApJ, 780, 9
Yang, H.-Y. K., & Reynolds, C. S. 2016, ApJ, 818, 181
Young, J. S., & Knezek, P. M. 1989, ApJL, 347, L55
Young, J. S., & Scoville, N. Z. 1991, ARA&A, 29, 581
Young, L. M. 2002, AJ, 124, 788
Young, L. M., Bureau, M., & Cappellari, M. 2008, ApJ, 676, 317
Young, L. M., Bureau, M., Davis, T. A., et al. 2011, MNRAS, 414, 940